Journal of Luminescence 287 (2025) 121473

Contents lists available at ScienceDirect

Journal of Luminescence

journal homepage: www.elsevier.com/locate/jlumin

Review

Lanthanide photonics on the path to future: from gas lighting to optical computers

Jean-Claude G. Bünzli [a,b,*], Ka-Leung Wong [a]

[a] Hong Kong Polytechnic University, Department of Applied Biology and Chemical Technology, Hung Hom, Hong Kong SAR, PR China
[b] Swiss Federal Institute of Technology, Lausanne (EPFL), Institute of Chemical Sciences and Engineering, Lausanne, Switzerland

ARTICLE INFO

Keywords:
Lanthanides
Photonics
Luminescence
Review
Applications
History

ABSTRACT

In 1891, Austrian scientist and entrepreneur Carl Auer von Welsbach filed a groundbreaking patent for a cotton mantle impregnated with cerium-doped thorium oxide, which converted the light and heat of gas lamps into a brilliant white glow. This marked the birth of lanthanide photonics and phosphor chemistry—a field that now underpins countless essential technologies, from solid-state lighting to cancer phototherapy and quantum computing information processing. This perspective explores the remarkable scientific journey of lanthanide photonics, highlighting recent breakthroughs and key developments. We begin with a historical overview before delving into fundamental advances including quantum chemical models, antenna effect and energy transfer mechanisms, the design of inorganic phosphors, the influence of electric and magnetic fields, molecular and circularly polarized luminescence, upconversion processes, and quantum bits. The final section focuses on cutting-edge applications, such as solid-state lighting, photovoltaics, mechanoluminescence, and biomedical innovations (optical imaging, cancer diagnosis, and photodynamic therapy), while briefly touching on other emerging uses. Rather than providing an exhaustive review, this article offers a concise yet broad overview of the field, spotlighting pivotal contributions from the past decade. Our goal is to capture the dynamism and interdisciplinary impact of lanthanide photonics as it continues to shape science and technology.

1. Out of darkness

1.1. Carl Freiherr Auer von Welsbach

When Carl Freiherr Auer von Welsbach (1858–1929) [1], a brilliant Austrian scientist and entrepreneur, obtained a patent for a gas mantle made of cotton impregnated with thorium oxide (thoria) doped with 1 % of cerium oxide (ceria) in 1891, he probably did not foresee the tremendous developments in lanthanide photonics we are presently experiencing, despite his deep intuition and practical insights. He (re-) opened a chemical factory the same year and started producing these mantles that were immediate success: in 1893, dividends of 130 % were paid to the investors of the company! The year 1891 can therefore be considered as the founding year of lanthanide photonics and the gas mantle the first lanthanide phosphor. Indeed, the device rapidly became essential to then ubiquitous gas lighting because it transformed the yellowish gas flame into brilliant white light with characteristics close to sunlight and were cheaper than electric bulbs; in 1913 alone, 300 million of mantles were produced and an estimated total of 5 billion were sold until the mid-1930s when electricity progressively replaced gas lighting. In fact, it was Auer's second attempt, the first one initiated in 1885 having been a failure because the first incandescent mantles he developed, based on zirconium and lanthanum oxides, emitted a cool greenish light for which ladies complained it changed the color of their faces! As a consequence, the factory opened in 1887 had to be closed two years later [2].

With the mass production of gas mantles, Auer was left with piles of other rare earths and was eager to find a use for them. He then reminded his time in Heidelberg with Professor Robert Bunsen when he was working on fused salt electrolysis for producing metallic rare earths. He had noted that when filing the rim of the crucible on which a deposit of mixed metallic rare earths and iron had formed, brilliant sparks were produced by triboluminescence. This was the inspiration for creating the pyrophoric alloy he called "mischmetal" and that enabled him to realize his dream of having a cheap and straightforward way of igniting gas lamps. A patent followed suit and was accepted in 1903; however, commercial application took five more years to develop. First the composition of the mischmetal had to be optimized for the best

* Corresponding author. Hong Kong Polytechnic University, Department of Applied Biology and Chemical Technology, Hung Hom, Hong Kong SAR, PR China.
E-mail addresses: jean-claude.bunzli@epfl.ch (J.-C.G. Bünzli), k.l.wong@polyu.edu.hk (K.-L. Wong).

https://doi.org/10.1016/j.jlumin.2025.121473
Received 24 May 2025; Received in revised form 4 July 2025; Accepted 14 August 2025
Available online 22 August 2025

pyrophoric effect: 30 % of iron and 70 % of a lighter rare-earth mixture (mainly La, Ce). But the resulting material was porous and highly brittle so that a means had to be found to eliminate the pores arising from phosphorous and oxychloride impurities. In 1908, 800 kg of adequate "Auer metal" were produced and processed into four million corrosion-resistant lighter flints. The same year, Auer created the "Treibacher Chemische Werke" (nowadays "Treibacher Industrie AG") that subsequently also manufactured pocket lighter flints. Mischmetal remained the main product of the company until the 1930s. Interestingly, this invention represents the first attempt to deal with the imbalance problem that rare earth extraction and production companies are facing, *i.e.* the ore composition does not match the demand for individual rare earths [3,4]. Auer was also a clever businessman. The rare earths he was using were extracted from sands in Brazil and at that time, fret ships carrying European goods to South America used to return empty. To stabilize them they had to carry ballast. Somehow Auer succeeded in convincing one of the shipping companies to use rare-earth containing sand as ballast, so that for several years he was getting his raw material free of charge, until the Brazilian government noted the practice and imposed taxes!

Therefore, in 1908, the first two industrial applications of rare earths were commercially available (Fig. 1), and both involved light, with a main characteristic when it comes to inorganic phosphors: the crucial role of dopants and impurities. In addition, and most importantly, the Auer mantle was saving 60–70 % of energy compared with the simple gas lamps it was replacing, prefiguring the energy savings cashed in when electric bulbs were replaced with rare-earth containing fluorescent lamps in the 1970s and, later in 1996, lanthanide-containing light-emitting diodes, as well as the present role of rare earths in the development of green energies. Both devices, the mantle and the lighter flint, are still available today but silk or other fabrics often replace cotton in the former and non-radioactive yttria, or zirconia are substituted for thoria. However, the mechanisms involved in light emission of these two devices have little connection with the electronic structure of the lanthanide ions, an aspect dealt with in the next story.

1.2. *The puzzle of rare-earth spectra [5]*

The invention of the spectroscope by Joseph von Fraunhofer in 1814 provided a practical tool for studying light emission and for identifying new elements. The sharp emission lines from lanthanide (Ln) salts and oxides drew the attention of several scientists in the mid-1860s, Robert Bunsen, William Crookes for instance, who relied on them for detecting new Ln elements in minerals. Several sensitive methods were being used, including spark spectroscopy – induced by electric sparks, cathodoluminescence, and phosphorescence. This led to the characterization of several new lanthanide elements [6] and, also, to accumulation of sizeable amount of spectroscopic data. However, despite that at the beginning of the 20th century most rare earths were available in reasonable purity, spectroscopists were having a hard time in deciphering the origin of their multiple emission lines [7].

Lanthanide elements are highly electropositive and form stable trivalent ions with electronic ground configurations $[Xe]4f^{n}$ (n = 0, La to 14, Lu) in which the 4f electrons are shielded by the filled $5s^{2}5p^{6}$ subshells. Other oxidation states are also reachable, in particular +2, for which organometallic complexes have been isolated for the entire series [8], or +4, mainly for Ce [9] and, to a lesser extent, for Nd, Pr, Tb, and Dy [10]. Divalent ions adopt one of two electronic configurations, $[Xe]4f^{n'}$ or $[Xe]4f^{(n'-1)}5d^{1}$ while tetravalent ions usually have $[Xe]4f^{n''}$ configurations. These electronic configurations are split by electron repulsion (quantum numbers S,L), spin-orbit coupling (quantum number J), and ligand-field (LF) effects, generating a wealth of electronic levels [11]. Globally, in low symmetry, the ground electronic configurations $[Xe]4f^{n}$ of all lanthanides can be split in a total of 1641 SLJ levels and 16 384 LF sublevels while the excited $[Xe]4f^{(n-1)}5d^{1}$ configurations yield 180 199 levels (Fig. 2) [12], a real playground for spectroscopists! Concentrating on the metal ion only, there are two different types of transitions: sharp intraconfigurational f-f transitions, the electric dipole

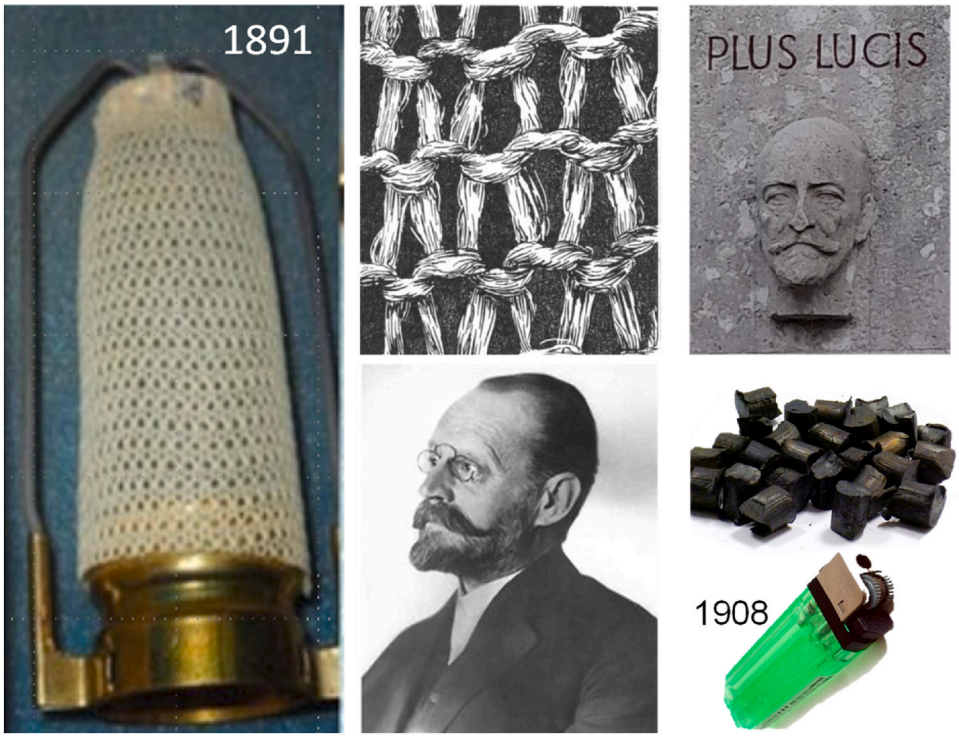

Fig. 1. Clockwise from left: Auer gas mantle; silk structure used in some gas mantles; "more light" Latin inscription on the base of a statue dedicated to Auer in front of the Chemisches Institut, Universität Wien; mischmetal (Wikipedia); modern lighter; Carl Auer von Welsbach (Bildarchiv der Österreichischen Nationalbibliothek, Wien).

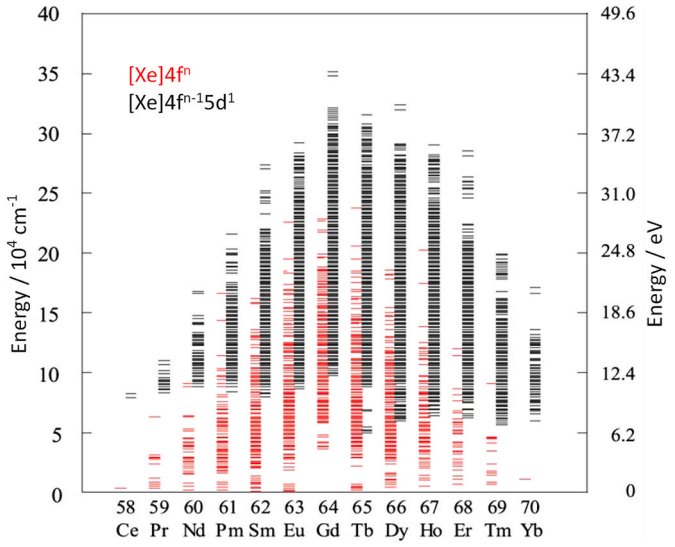

Fig. 2. Calculated energy levels for the [Xe]$4f^n$ (red, left scale) and [Xe] $4f^{(n-1)}5\ d^1$ (black, right scale) electronic configurations of Ln^{3+} ions (red, left scale); ligand-field splitting is not considered. Note that the right scale is in eV (1 eV = 8066 cm^{-1}). Reproduced with permission from Ref. [12] © 2007 Elsevier B.V.

contributions of which are forbidden by Laporte's rule (magnetic dipole f-f transitions are allowed, but quite faint), and broader and allowed f-d transitions; for Ln^{3+} ions, the latter occur in the UV, above 50 000 cm^{-1}, except for Ce, Pr, and Tb for which ligand-field splitting may shift these transitions into the visible range. In addition, allowed, broad and intense ligand-to-metal charge transfer transitions also usually appear above 50 000 cm^{-1}, except for Eu^{3+} and Yb^{3+} (Fig. 3). Examples of 4f-4f and 5d-4f transitions are displayed in Fig. 4.

In the wake of the development of quantum mechanics and chemical bonding theories in the 1920s, Bethe proposed in 1929 the crystal-field (CF) theory (later expanded to ligand-field (LF) theory) to explain the bonding in inorganic metal-containing solids. At that time, the ground electronic configurations of trivalent lanthanides were also established. However, their spectra remained mysterious, particularly when it came to explaining why some lines were faint and sharp, and other broad and more intense. The conundrum was finally solved by John H. van Vleck who published a seminal paper in 1937 [5] addressing two main issues: (i) what is the origin of the sharp *vs* broad lines and (ii) why are the sharp faint lines observed at all? Considering the first interrogation, Van Vleck

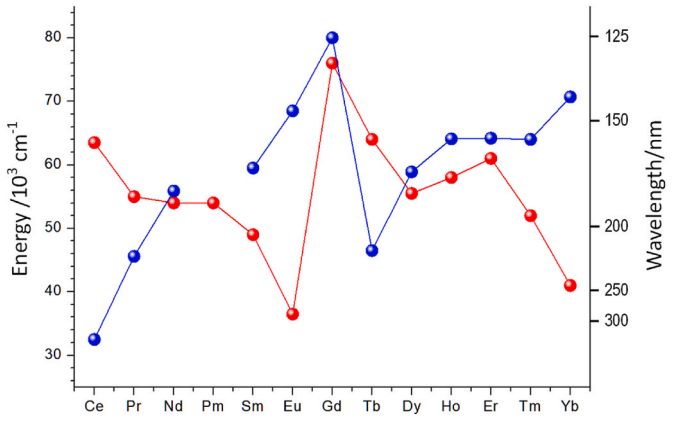

Fig. 3. Experimental energies of the first spin-allowed 4f→5d transitions of trivalent lanthanides doped in CaF_2 (blue balls) and calculated energies of the O (2p)-to-Ln^{3+} charge transfer transitions (red balls). Graph created using data from Refs. [13,14], respectively.

correctly assigned the sharp lines to intraconfigurational 4f-4f transitions and, most importantly, stated that the most intense ones were having electric dipole character; he then also assigned the broad bands observed in the spectra of Ce^{3+} and Yb^{3+} to interconfigurational 4f-5d transitions. Although correct for cerium, this assignment was not accurate for ytterbium for which 5d-levels lie at energies higher than 70 000 cm^{-1} (Fig. 3); the correct assignment is a charge transfer transition. The second point was trickier to explain, but Van Vleck postulated that formally forbidden electric dipole intraconfigurational 4f-4f transitions are observed because of a "distortion of the electronic motion by crystalline fields", which is indeed one of the mechanisms invoked today for explaining the intensity of these transitions (f-orbital mixing with ligand orbitals). Furthermore, he established that this distortion only occurs if the ligand field is devoid of an inversion center; in the presence of such a symmetry element, orbital mixing is not allowed. Finally, Van Vleck also realized that interaction between f-electronic levels and vibrations results in additional "vibronic" components in the spectra and/or in broadening of some lines. The paper by Van Vleck represents a major advance in lanthanide spectroscopy and it paved the way for the works of Gerhard H. Dieke [17], Brian Wybourne [18], and William T. Carnall [19–22] on electronic level diagrams and of Brian R. Judd [23] and George S. Ofelt [24] on the theory rationalizing the intensity of the intraconfigurational f-f transitions. It is worth noting that detailed elucidation of lanthanide electronic spectra remains difficult, in particular because of temperature effects on the population of ligand-field sublevels [25].

1.3. *Scope of this perspective*

Lanthanide photonics is at the heart of applications as diverse as economical solid-state lighting, laser materials, telecommunications, displays, security inks and tags, pressure sensors, luminescent thermometers, assistive technologies, bioanalyses, bioimaging, cancer radiotherapy and phototherapy. Recent developments have seen its outreach extending to futuristic technology, such as optical cooling, or qubits for atomic clocks and optical computers. In this perspective, several aspects of this dynamic and breathtaking science are highlighted, for instance advances in theory and energy transfer modeling, or present applications, while pointing on emerging and/or unusual ones. Each section is treated as a synopsis, focusing on a few recent contributions of the past decade and does not consist, by far, of a comprehensive review of the subject, the reader being referred to relevant review articles, whenever available.

2. Fundamentals

2.1. *Quantum chemical models*

Luminescence arises from the reorganization of the electronic structure of the emitting species, making a deep understanding of its mechanisms dependent on detailed knowledge of both ground and excited-state electronic configurations. Theoretical modeling approaches vary in complexity, depending on the specific properties under investigation. For a comprehensive and accurate description of the electronic properties of lanthanide compounds and materials, advanced computational methods are now available, thanks to significant advancements in computer technology. These advancements have enabled faster calculations and the ability to handle systems with a large number of atoms. Among these methods, *ab initio* and time-dependent density functional theory (TD-DFT) calculations are increasingly employed, despite the inherent challenges posed by 4f-elements.

The electronic structure of lanthanide ions, characterized by an open 4f shell, along with relativistic and polarization effects, makes computational modeling particularly complex. This complexity escalates significantly when moving from free ions to molecules, solid-state structures, and nanoparticles. Over the past decade, substantial efforts

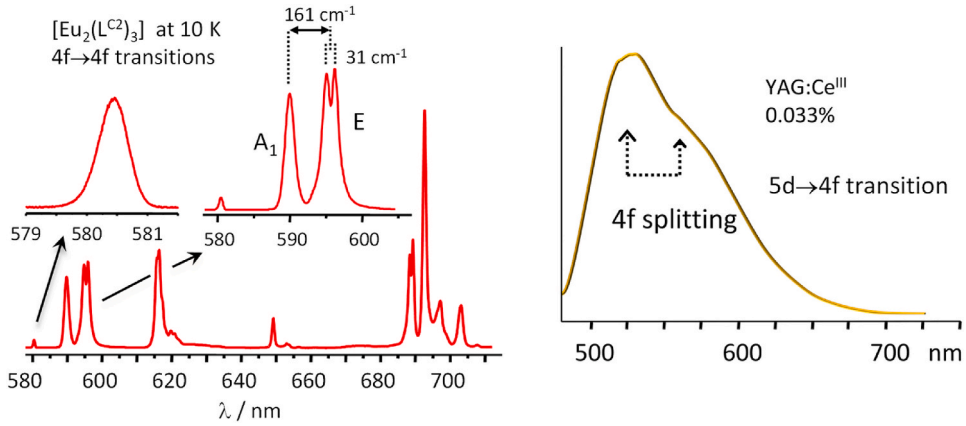

Fig. 4. Typical lanthanide emission spectra. Left: 4f-4f transitions of an Eu^{3+} helicate having approximate D_3 symmetry; the right insert shows the LF splitting of the $^7F_1$ state, and the small splitting of the E component is evidence for a distortion of the coordination polyhedron towards C_2 symmetry; adapted from Ref. [15]. Right: $^2D_{3/2} \rightarrow {}^2F_{7/2,5/2}$ transition of Ce^{3+} doped at 0.033 % in $Y_3Al_5O_{12}$, a phosphor used in 1st generation of white light-emitting diodes (WLEDs); adapted from Ref. [16].

have been made to refine the basis sets for 4f-orbitals, which are critical for accurately representing electronic wave functions in computational studies. The level of approximation in these basis sets directly impacts both the accuracy of calculated parameters and the computational cost. With modern computing capabilities, fewer compromises are necessary, and relativistic effects are now routinely incorporated into effective core potentials (ECPs), also known as pseudopotentials (PPs). These PPs model core electrons using a potential that accounts for spin-orbit interactions, while 4f electrons are treated as part of the valence shell. Notably, 4f-in-valence optimized PPs have been developed [26]. However, these calculations remain computationally expensive, and achieving convergence is often challenging. To address this, M. Dolg et al. proposed integrating the radially contracted 4f-electrons—shielded by the $5s^25p^6$ subshells—into the core potential [27] (Fig. 5). This approach includes both non-relativistic and quasi-relativistic energy-consistent parameters and is compatible with ligand-field theory [28].

Further progress has been made in reducing computational costs, particularly in addressing the cubic scaling of calculations with respect to system size. This limitation previously restricted practical calculations to systems with fewer than N~100 atoms. A significant breakthrough came with the development of separable pseudopotentials, such as the Goedecker-Tetter-Hutter (GTH) pseudopotentials, which reduce the scaling to N^2 [29]. Building on these advancements, Jun Li et al. recently introduced norm-conserving 4f-in-core pseudopotentials and valence-shell Gaussian basis sets [30]. These models treat the core as comprising 46 electrons ([Kr]4 d^{10}) plus the n 4f electrons (Fig. 5). The proposed parameters were tested on lanthanide halides (LnX_3, where X = F, Cl, Br), aquo ions (with coordination numbers of 8 and 9), and aqueous solutions of complexes with small ligands. The results demonstrate reasonable accuracy in reproducing binding energies and Ln-to-ligand distances. While some transferability issues remain, these PPs and basis sets enable large-scale calculations and molecular dynamics simulations for complex lanthanide systems.

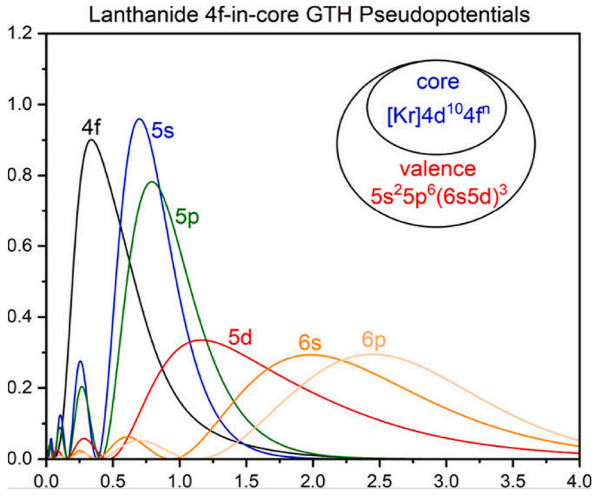

Fig. 5. Radial distribution probability densities $D(r) = r^2R(r)^2$ for 4f, 5s, 5p, 5d, 6s, and 6p orbitals of Nd atoms with the ($[Kr]4d^{10}5s^25p^66s^24f^45d^06p^0$) configuration; $R(r)$ is the radial wavefunction. Reproduced with permission from Ref. [30] © 2023 American Chemical Society.

For simpler modelling approaches that align closely with experimental observations, crystal-field and ligand-field theories have been widely employed to interpret the emission spectra of lanthanides. These theories remain highly convenient and conceptually straightforward tools for understanding lanthanide luminescence [31]. When it comes to predicting oscillator strengths, the semi-empirical Judd-Ofelt (JO) theory, developed in 1962 within the framework of CF theory, continues to be a cornerstone in lanthanide optical spectroscopy [32]. Despite its simplified initial assumptions, this three-parameter model successfully reproduces the intensities of absorption and emission spectra for many lanthanide ions. It also offers valuable insights into nature and strength of interactions between lanthanide ions and their surrounding ligands. Derived quantities from the JO theory – such as radiative lifetimes, branching ratios, stimulated emission cross-sections, luminescence quantum yields, and sensitization efficiencies – offer a comprehensive characterization of the emissive species.

The Judd-Ofelt theory is particularly well-suited for analyzing europium luminescence. This is due to the presumed purely magnetic nature of the $^5D_0 \rightarrow {}^7F_1$ transition, which is often used as an internal reference because its intensity is theoretically independent of the Eu^{3+} environment (though this assumption has been debated [33]). To facilitate the application of this theory, a freely available software tool called JOES has been developed for analyzing Eu^{3+} emission spectra [34]. JOES calculates the aforementioned parameters, generates CIE chromaticity coordinates, and evaluates the site symmetry of the emitting species. In 2021, a free-of-charge web platform, termed JOYSpectra [35], expanded the capabilities of JOES to most Ln^{3+} ions. It calculates and analyses the JO intensity parameters and evaluates intramolecular energy transfer rates from excited donor states up to 310 transitions involving 12 Ln^{3+} ions (Ln = Pr-Yb). There is no need to install the program, calculations are made online, and results are sent to the operator by e-mail. The web platform is constantly updated and designed to be user-friendly for experimentalists and theoreticians interested in analysis of the photophysical behavior of lanthanides. On

the other hand, it does not calculate or optimize the geometry of the complexes that has consequently to be input, either under the form of Cartesian coordinates or as output of programs such as Gaussian, Orca, or MOPAC. The package is illustrated by convincing calculation of the energy transfers and quantum yields for $[Ln(tta)_3(H_2O)_2]$ (tta is thenoyl-trifluoro-acetylacetonate; Ln = Eu, Tb). The main calculation steps and functionalities of JOYSpectra are shown in Fig. 6.

2.2. Understanding energy transfer mechanisms in the antenna effect

Turning our attention to the brightness of lanthanide luminescent compounds and probes [36], significant developments have focused on understanding the *antenna effect* – the sensitization of lanthanide ion luminescence through energy transfer from their surrounding environment. To appreciate these advancements, it is instructive to examine how and when various models were developed.

The foundation for understanding intramolecular energy transfer in lanthanide complexes was laid in 1961 by M. A. Crosby et al., who proposed a model involving energy transfer from the lowest triplet state (T_1) of the organic ligand to the emitting excited state of the trivalent lanthanide ion [37]. This model was further substantiated in 1969 by M. Kleinerman, who studied over 600 chelates and demonstrated that when the energy of T_1 is lower than the emitting Ln^{3+} level, sensitization occurs via the excited singlet state (S_1) [38]. The following year, S. Sato and M. Wada conducted a seminal photophysical study of Eu^{3+} and Tb^{3+} chelates, employing time-resolved spectroscopy to reveal that initial excitation for Eu^{3+} occurs in the $^5D_1$ emitting state, which subsequently transfers energy to the $^5D_0$ state [39]. This finding was supported by the larger spectral overlap for the $^5D_1$ state. Their work also included detailed kinetic models, incorporating multiple rate equations, and established a correlation between the quantum yield and the energy gap (ΔE_{gap}) between the 0-phonon component of the triplet state and the $Eu^{3+}(^5D_1)$ level, as a function of temperature.

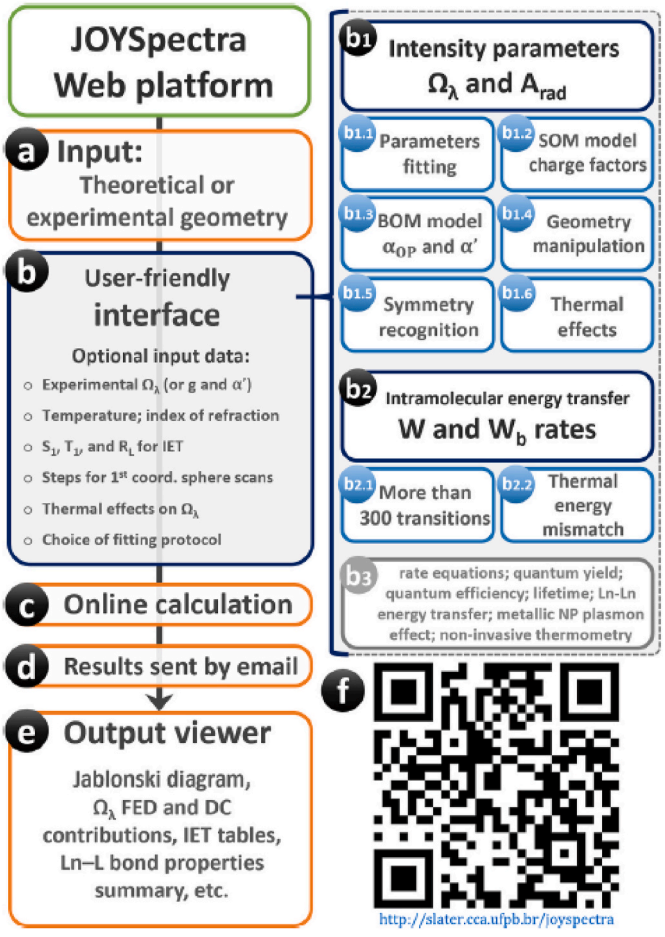

Fig. 6. Main functionalities and flow diagram of the web platform JOYSpectra. For precise definitions, please refer to Ref. [35]. Reproduced with permission from Ref. [35], © 2021 Elsevier B.V.

During the 1990s–2010s, several researchers revisited and expanded these ideas, focusing on the **S_1-T_1-Ln*** model for Eu^{3+} and Tb^{3+} complexes. They proposed simplified "golden rules" for the energy gaps ΔE_{gap} and for $\Delta E(S_1\text{-}T_1)$. However, these studies often overlooked the earlier works described above and failed to account for the complexity of energy transfer mechanisms, which are unique for each Ln^{3+} ion. Moreover, these earlier models neglected the critical role of non-radiative deactivation pathways, such as vibrational quenching or photoinduced electron transfer, or quenching by intermolecular or intramolecular charge transfer states [40], which can significantly impact luminescence efficiency. They also failed to account for the fact that several electronic mechanisms can operate and that the distinction between singlet, triplet and charge transfer states is not as clear-cut as some of these states may mix. It is now evident that these oversimplified models and their associated "golden rules" are inadequate for capturing the intricate dynamics of energy transfer in lanthanide chelates. Moving forward, more realistic and comprehensive models are needed to better understand and predict the luminescent behavior of lanthanide-based systems.

A completer and more workable model for describing the antenna effect was only set out at the beginning of the century by Brazilian researchers [41,42] who later proposed an open-access software package for the Windows operating system, LUMPAC [43]. This model includes several aspects, in particular it takes into account the various mechanisms by which energy can be transferred, namely exchange (Dexter), dipole-dipole (Förster), dipole-2^λ-multipole mechanisms, as well as several donor states from the ligand (singlet, triplet, charge transfer states) and several acceptor states of the lanthanide. A full kinetic model is also established to reflect energy migration within all these states and corresponding rate constants are calculated. The workflow of this program is as follows.

❖Optimization of the ligand geometry using the Austin 1 procedure (AM1) or other more performing calculations like parametric models PM3, PM6, or PM7, all working within the frame of the Neglect of Differential Diatomic Overlap (NDDO) scheme. The calculation procedures are constantly updated.

- ❖ Optimization of the complex geometry using the Sparkle model within the Molecular Orbital Package (MOPAC) program, *i.e.* a central Coulomb potential with the Ln^{3+} ion replaced with a +3e point charge and coupled with one of the AM1 or PMx procedures. Recent improvement uses the RM1 model for the Ln^{III} (Ln = Eu, Gd, Tb) ions: the {[Xe] $4f^n$} electronic configuration is described by the effective core potential with the RM1 core charge of the lanthanide set as +3*e*. The semi-empirical basis set used is composed of 5d, 6s, and 6p orbitals. With this model, Ln-X (X = C, N, O, S, Cl, Br) bond lengths can be predicted within ±0.06 Å.
- ❖ Calculation of the ligand excited states and transition probabilities with Zerner's Intermediate Neglect of Differential Overlap (ZINDO) program.
- ❖ Evaluation of the JO intensity parameters from the emission spectrum of Ln^{3+} with the simple overlap model (SOM) for the odd-component of the ligand-field and the dynamic coupling mechanism for the contributions of ligand polarizability. Covalency effects are not considered explicitly, and the calculation is limited to two JO parameters only, Ω_2 and Ω_4.
- ❖ Laying out a kinetic model of energy transfer considering the relevant ligand and Ln^{3+} states (chosen by considering their respective energy and potential overlap), back transfer, as well as several energy transfer mechanisms. Calculations have shown that dipole-

quadrupole transfers may contribute substantially to the overall process, especially for electric-dipole (ED) forbidden transitions. Selection rules have also to be considered [44]: $|J - J'| < \lambda \leq |J + J'|$ for dipole-dipole and dipole-multipole transfer ($\lambda = 2, 4, 6$) and $|J - J'| = 0, \pm 1$ for exchange transfer; 0-0 transfers are excluded. These rules hold for pure orbitals and J-mixing can relax them, fortunately. In the case of Eu^{3+} for instance, direct ED excitation of $^5D_0$ from $^7F_0$ is forbidden by Laporte, ΔS, ΔL, and ΔJ selection rules (magnetic dipole (MD) excitation is allowed), but J-mixing, which can be estimated by the intensity ratio between $^5D_0 \rightarrow {}^7F_0$ and $^5D_0 \rightarrow {}^7F_2$ transitions, effectively makes transfer to $^5D_0$ possible. Moreover, the $^5D_0 \leftarrow {}^7F_1$, $^5D_1 \leftarrow {}^7F_0$, and $^5D_1 \leftarrow {}^7F_1$ transitions are partially MD allowed; the population of $^7F_1$ at room temperature is about 25–30 % so that this level is an important factor in the transfer process as well as $^5D_1$; once excited the latter rapidly and mostly relaxes to $^5D_0$.

This software is now standard for many researchers. However, it does not solve all the problems associated with the sensitization of lanthanide ion luminescence. Indeed, vibronic interactions are not taken into consideration. In an effort to alleviate this situation, the role of vibronic coupling in the dynamics of the S_1-to-T_1 intersystem crossing (ISC) in Eu^{3+} complexes has been analyzed and a correlation function formalism established by considering vibronic coupling effects originating from the vibrational density of states [45]. After optimization of the geometry of the ground, S_1, and T_1 states by DFT and TD-DFT, the dynamics of the ISC is captured by normal mode analysis followed by local vibrational mode analysis. The calculated ISC rates for four Eu^{3+} complexes align much better with the measured ones compared to semi-empirical calculations previously used. A noteworthy finding is that coupling with vibrations in the 700-1600 cm^{-1} range leads to faster ISC, and local vibrational analysis shows this process being driven by delocalized vibrations across the molecule. Therefore, tailoring the ligand framework may be an efficient tool for producing faster ISC.

In 2017, M. Dolg, X. Chen & coll. have proposed an alternative model for the energy transfer scheme leading to the antenna effect in europium chelates: the energy resonance crossing (ERC) model, controlled by nonet-quintet intersystem crossing [46]. The model, based on multi-configurational quantum-chemical approach with relativistic energy consistent ab-initio pseudopotentials, was initially developed for explaining the large quantum yield difference observed between $[Eu(L^1)_2]^-$ ($Q = 0.22$) and $[Eu(L^2)_2]^-$ ($Q = 0.062$), where L^1 and L^2 are 1-hydroypyridin-2-one (1,2-HOPO) derivatives (Fig. 7, top). The Dexter/Förster/dipole-2^λ-pole mechanisms for which the donor-acceptor distance is decisive cannot account for this difference. The new model shows that the photoexcited ligands undergo rapid relaxation to their charge-transfer states, followed by ISC to triplet states. The presence of Eu^{3+} significantly alters the surface topology, leading to near singlet-triplet degeneracy and facilitating efficient $^9(^3\pi\pi^*/{}^7F_0) \rightarrow {}^5(S_0/{}^5D_1)$ energy transfer (Fig. 7, bottom). The resonant energy transfer mechanism involves the degeneracy of nonet and quintet states, which allows for efficient energy transfer from the ligand to the Eu^{3+} ion. This process is mediated by strong spin-orbit coupling, which enhances the ISC rates and leads to the population of the emissive states of Eu^{3+}. The higher quantum yield for the L^1 chelate is satisfyingly explained as arising from better resonance conditions and stronger spin-orbit coupling.

Later the model was applied to Eu^{3+} chelates with 1-phenyl-3-pyridin-3-yl-propane-1,3-dione (PPPD) and 1-(n-bromophenyl)-3-(pyridin-3-yl)propane-1,3-dione (n = 3, 4) and validated with time-resolved luminescence measurements showing the following sequence in emission: ligand fluorescence – nonet state phosphorescence – quintet state emission – $Eu(^5D_0)$ emission [47]. Furthermore, the model has been recently complemented by adding internal conversion (IC) paths ($^1\pi\pi^* \rightarrow S_0$) and expanding it to complexes of other trivalent lanthanides (Ce, Nd, Sm, Eu, Gd, Tb, Ho, Er, Yb) featuring anthracene as antenna [48]. As shown in Fig. 8, the leading energy paths in the energy transfer

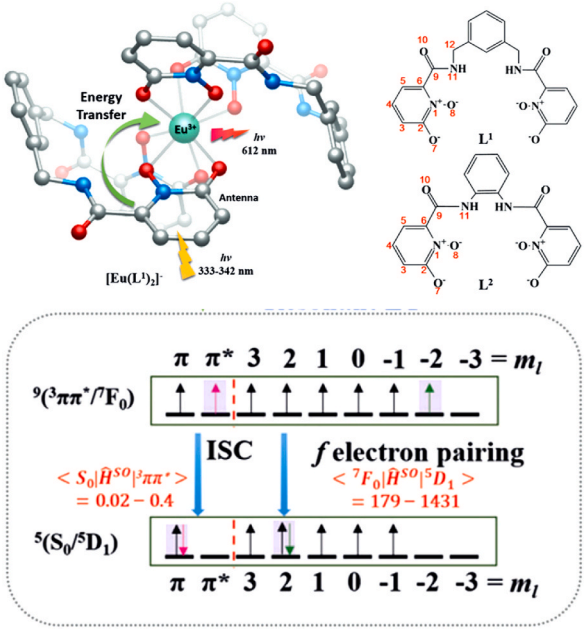

Fig. 7. Left: ligands for the studied $[Eu(L^n)_2]^-$ chelates, structure of $[Eu(L^1)_2]^-$. Right: Minimum energy profiles of the resonance energy transfer in $[Eu(L^1)_2]^-$ chelate from CASPT2/IRC/CASSCF level of theory. Values of the sin-orbit matrices are in cm^{-1}. Reproduced with permission from Ref. [46] © 2017, Wiley Interscience.

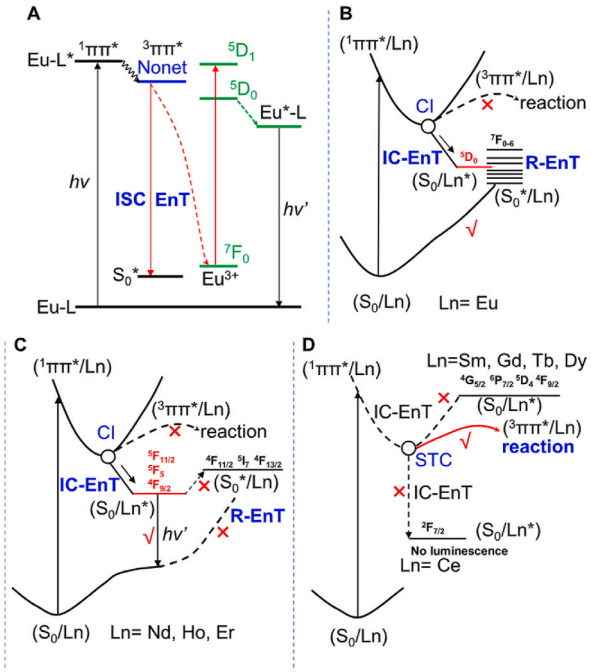

Fig. 8. ISC-driven (A) and IC-driven (B, C, D) resonant energy transfer paths for various trivalent lanthanide ion in complexes with an anthracene antenna. Reproduced with permission from Ref. [48] © 2024 American Chemical Society.

process depend on the nature of Ln, and four situations are described that combine IC-driven ($^1\pi\pi^* \rightarrow S_0$) and ISC-driven ($^3\pi\pi^* \rightarrow S_0$) resonant energy transfer.

2.3. Inorganic phosphors

Lanthanide inorganic phosphors are vital materials in modern technology in view of their exceptional luminescent properties. These materials are widely employed in diverse applications, including solid-state lighting, display technologies, food production, anticounterfeiting measures, photovoltaics, and medical imaging and therapy. Their versatility and performance have spurred a significant volume of scientific and technical research in recent years. Current efforts are directed toward enhancing their efficiency, stability, and cost-effectiveness. Key areas of focus include the development of broad-band excitation strategies, the exploration of innovative host materials, the optimization of doping concentrations, and the advancement of novel synthesis protocols. Nanostructures, especially upconversion nanoparticles (UCNPs), are emerging as the cornerstones of the field, particularly since P. Zhang et al. demonstrated their usefulness in photodynamic therapy of cancer in 2007 [49], and several breakthroughs have been achieved using them for nanothermometry as well as cancer and COVID-19 diagnostics during the past decade.

2.3.1. Influence of the temperature on UCNP luminescence

One of the drawbacks of UCNPs is their low quantum yield and brightness although substantial improvements are being recorded. Temperature is a key factor in this respect and usually, the interplay between light and heat leads to the well-known luminescence thermal quenching effect. This effect is often related to vibrations and short-range electronic-to-vibrational energy transfer (EVET) can be quite effective, though undesired. The major parameters governing the efficiency of EVET are (i) the overlap between the emission spectrum of the Ln^{3+} ion and the absorption spectrum of the vibrations and/or their combinations and harmonics, (ii) the oscillator strengths of the implied transitions, and (iii) the density of EVET acceptors in a volume that can extend to several nm from the NP surface; mechanisms for this type of quenching are starting to be understood [50]. However, it turns out that in some UCNP materials, temperature has an opposite effect. Sometimes it may simply arise from the evaporation of adsorbed water molecules on the surface of the NPs, but other phenomena have been observed; for instance, in the ubiquitous $NaYF_4$:Yb^{3+},Er^{3+} material for which the upconversion luminescence intensity increases in the range 4–100 K. The UCL emission is sensitized by the Yb($^2F_{5/2}$) crystal-field multiplet and the most efficient energy transfer occurs from the higher Yb($^2F_{5/2}|0\rangle$) state to the Er($^4I_{11/2}$) state. Increasing the temperature results in increasing the population of the Yb($^2F_{5/2}|0\rangle$) sublevel, therefore a better sensitization [51]. In large UCNPs of this material, normal thermal quenching is observed above room temperature. However, smaller UNCPs show an anomalous thermally induced UCL enhancement that is inversely proportional to the size of the NPs [52]. Small $NaYF_4$:Yb^{3+}, Tm^{3+} UCNPs present the same behavior. A detailed analysis demonstrated that the "dark" layer of inactive sensitizers and activators at the surface of the NPs can be illuminated by an oxygen moiety coordinated to the Yb^{3+} ions; the formation of the Yb…O bonds favors energy transfer and a 3000-fold enhancement of Tm^{3+} blue UCL emission was recorded [53]. The phonon generated at the surface of the nanomaterials can therefore break the limitation commonly encountered in producing UCL, as further demonstrated for $NaYF_4$:Yb^{3+},Nd^{3+} nanoparticles surface-coated with oleic acid [54]. Fig. 9 depicts the three enhancement mechanisms, moisture release, host phonon and surface phonon assistance, and shows the contribution of each in 10-nm NPs coated with OA and OA free for comparison. It is noteworthy that the phenomenon is perfectly reversible.

2.3.2. Broad-band sensitized lanthanide nanoparticles

The two worlds of inorganic phosphors and organic dyes/luminescent chelates have long ignored each other. But the stringent limitations inherent to UCNPs have triggered scientists trying to overcome the Shockley–Queisser efficiency limit of 32 % of a single-junction solar cell

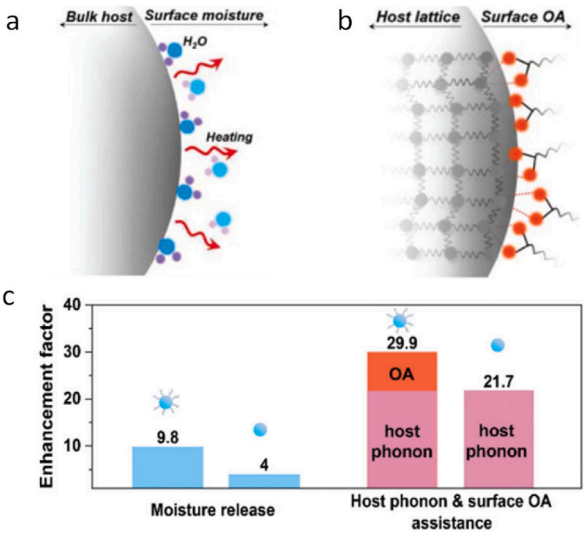

Fig. 9. Role of moisture release, host phonon assistance, and surface phonon assistance in oleate acid (OA) capped and OA free 10-nm β-$NaYF_4$:Yb^{3+},Nd^{3+} nanoparticles. a) Schematic of moisture release, b) schematic of phonon assistance from both host lattice and active surface, c) Analysis of the enhancement factor due to the three mechanisms; left: capped and right: OA-free NPs. Redrawn with permission from Ref. [54], © 2019 The Royal Chemical Society.

by using upconversion materials to introduce the concept of dye-sensitized UCNPs in 2012 [55]. This concept was rapidly applied to other types of nanoparticles, downshifting (DSNP), downconversion (DCNP) nanoparticles, and was extended to the interaction between NPs and dyes in which the energy donors are the nanoparticles [56]. There are two advantages resulting from the connection between dyes and lanthanide NPs: (i) the much larger cross section of the organic dye compared to absorption cross sections of Ln^{3+} ions combined with the large number of dye molecules connected to the NP (usually 50–100/NP), and (ii) the absorption time; Ln^{3+} ions have long excited state lifetime (μs-ms) so they need time to return to the ground state, during which they do not absorb; this is not the case for organic materials that have fluorescence lifetimes in the ns range.

The outcome of dye/NP coupling can be remarkable. For instance, very small Ln_2O_3 NPs (~2 nm) grafted with poly(acrylic) acid (PAA) and with the organic sensitizer 2,6-pyridinedicarboxylate (PDA) dispersed in water feature absolute quantum yields of 87.6 (Ln = Eu), 73.6 (Tb), and 2.8 % (Dy) upon excitation in the DPA singlet state at around 285 nm. For Ln = Eu, Tb, these data represent 13-fold and 7.5-fold improvements, respectively, with respect to NPs devoid of the DPA coating [57], demonstrating the efficiency of the NP-dye coupling. When it comes to UCNPs, one can expect enhancements of approximately 4–5 orders of magnitude in the upconversion process and 3-4 orders of magnitude in the overall brightness. For visible absorbing dyes, *i.e.* for downshifting NPs, common organic compounds are fluorescein isothiocyanate or well-established ligands such as tropolonates, diketonates, dipicolinates, benzoates, to name but a few [55]. Attention however is more focused on IR-absorbing dyes and UCNPs, particularly for biomedical applications for which NIR-I and NIR-II biological windows are targeted. A wealth of NIR dyes are available, cyanine dyes absorbing between 500 and 800 nm, and IR-dyes (650–1100 nm) being the most popular compounds [55,58]. If the organic-dye/Ln^{3+} nanoparticle coupling generates large benefits with respect to brightness, their photostability remains a problem, photobleaching of the dye continuing to be important. The photodegradation occurs via *in situ* production of singlet oxygen which reacts with the unsaturated bonds of the dye. This problem starts to be addressed; for instance, J. Capobianco's group have derivatized the IR-820 dye coupled to $NaGdF_4$:Er^{3+},Yb^{3+}@$NaGdF_4$:Yb^{3+} UCNPs with the sterically hindering 4-nitrothiophenol group. This

resulted in decreasing the absorption of the red Er^{3+} emission by dye, increasing the spectral overlap with Yb^{3+} and improving the photostability of the dye-derivatized UCNPs. After 1h irradiation at 800 nm (4.5 W cm^{-2}), degradation of the dye has been reduced from 75 % to 45 % [59]. Although encouraging, this result is not completely satisfying so that the same group proposed another strategy. On one hand, the IR-820 dye was modified with a 4-mercaptobenzoic acid group and linked to the surface of the silica-coated $NaGdF_4$:Er^{3+},Yb^{3+}@$NaGdF_4$:Yb^{3+} UCNPs (designed by SL); on the other hand, IR-820 was connected to 3-aminopropyl trimethoxysilane (APTMS) and embedded in the silica coating of the UCNPs (designed by SE). The resulting photostability of the SE system is shown in Fig. 10 and is quite remarkable; moreover, this system is 50 % brighter than the corresponding SL one [60].

There are other ways of achieving broad-band excitation in Ln-containing NPs, for instance by using the d-f transitions of Ce^{3+} [61] or d-d transitions (*e.g.* Cr^{3+}, Mn^{2+}, Ni^{2+}) [62], or surface plasmon resonance effects [63]. These are not discussed here.

2.3.3. Photon avalanche

The phenomenon of photon avalanche was discovered in Pr^{3+}-doped LaX_3 (X = Cl, Br) crystals in 1979 by J. S. Chivian et al. who were investigating the infrared quantum counter process (nowadays called upconversion). In Chivian's experiment, the metastable level Pr($^3H_5$) is excited by a 4.5 μm radiation (ground-state absorption, GSA). The sample is simultaneously submitted to the green output of a continuous wave laser resulting in excitation of the Pr($^3P_1$) level (excited state excitation, ESA). At low pump power density, the Pr($^3P_1 \rightarrow {}^3F_2$), Pr($^3P_0 \rightarrow {}^3F_2$), and Pr($^3P_0 \rightarrow {}^3F_6$) transitions are observed but if the pump power density is increased above a given threshold (>1.5 W cm^{-2}), all transitions described in Fig. 11a are detected and their overall emission intensity jumps by more than two orders of magnitude, creating a photon avalanche (Fig. 11b) [64].

There are several key parameters required for obtaining large photon avalanche. The GSA must be very weak to keep a large fraction of non-excited ions; conversely, the ESA process must have large oscillator strength (typically 10^4 times larger than GSA) so that ions occupying the $^3H_5$ level are rapidly promoted. Then the ions in the upper excited state interact with non-excited neighboring ions and the energy is distributed between pairs of ions (cross relaxation, CR) with the result of doubling the number of excited ions. Finally, repetition of ESA/CR cycles generates more excited ions, each cycle doubling the number of excited ions, leading to emission of a photon avalanche (Fig. 11c). This means that the CR process must be very efficient and the concentration of the activator in the matrix material large. This last point was somewhat overseen until C. Lee et al. reported in 2021 photon avalanche in small, carefully engineered, $NaY_{1-x}Tm_xF_4$ nanoparticles with an optimum x = 8 % [65]. The slope of the emitted intensity versus the logarithm of the pump power over the avalanche steep region reaches values as high as 26! The kinetics and relative brightness of the NPs have been evaluated with a kinetic model of energy transfer processes that revealed upconversion quantum yield reaching 40 % (maximum is 50 % for upconversion) when the NPs are excited beyond the threshold, at 10^5 Wcm^{-2}. Such a model is important for the search for adequate materials displaying photon avalanche. An obvious application is photon-avalanche single--beam super-resolution imaging (PASSI) that has been performed by excitation at 1064 nm; single particles were imaged with a maximum spatial resolution of 70 nm obtained by scanning confocal microscopy, without computational analysis. One drawback though is the long rise time of the avalanche preventing monitoring dynamic biochemical processes. The search for adequate avalanche materials is a vivid subject, expanding to several lanthanide ions, as summarized in a 2024 review article [66]. It is noteworthy that a record non-linear response of 60th order has been reported for the upconverting core-shell-shell $NaYF_4$:Tm (8 %)@NaYF4:Yb(10 %),Tm(1 %)@$NaYF_4$ nanoparticles [67].

2.4. Influence of electric and magnetic fields

Light is a combination of perpendicularly oscillating electric and magnetic fields, therefore it is expected that when submitted to such fields, optical properties will be influenced [68], opening the door to an external control that is useful in optoelectronic devices, optical memories, displays, light-emitting diodes, or biomedical devices, for instance. Lanthanide materials are ideal for these types of applications in view of their specific luminescent properties.

2.4.1. Electric field modulation

Lanthanide-doped ferroelectric and semiconductor materials have gradually conquered the optoelectronic industry due to their ability to modulate their luminescence properties through electric fields. For instance, doping ferroelectric $LiNbO_3$ crystals and polarizing them with an electric field of 200 kVcm^{-1} leads to a six-fold increase in the Er^{3+}($^4I_{13/2} \rightarrow {}^4I_{15/2}$) fluorescence intensity [69]. Smaller electric fields induce smaller, although noticeable, effects, like in a Yb^{3+}-doped perovskite ferroelectric single crystal for which a 10 kVcm^{-1} external field amplifies the Yb^{3+} emission by 16.7 % consecutive to a polarization rotation of the 90° domain [70]. Reversible modulation of the luminescence of Eu^{3+} doped in SnO_2 nanocrystals (0.5 %) has been achieved by applying a ±30 V electric potential. Modulation occurs only when excitation is through the valence band-to-conduction band transition at 339 nm, but not directly into the $^5L_6 \leftarrow {}^7F_{0,1}$ transition. On the other hand, the photocurrent increases >10^3-fold, so that the luminescence intensity decrease upon an applied positive potential is due to a decrease in recombination of the photogenerated charge carriers; when the

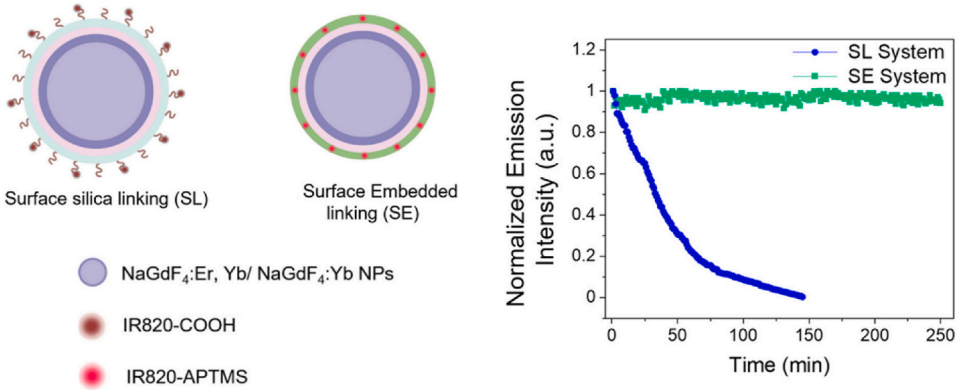

Fig. 10. (Left) schematic representation of the two $NaGdF_4$:Er^{3+},Yb^{3+}@$NaGdF_4$:Yb^{3+}@SiO_2 systems with derivatized dye IR-820 linked to the silica surface (SL) or embedded into the silica shell (SE). (Right) Normalized emission intensity versus time upon 808-nm irradiation. Redrawn with permission from Ref. [60] © 2023 The Royal Society of Chemistry.

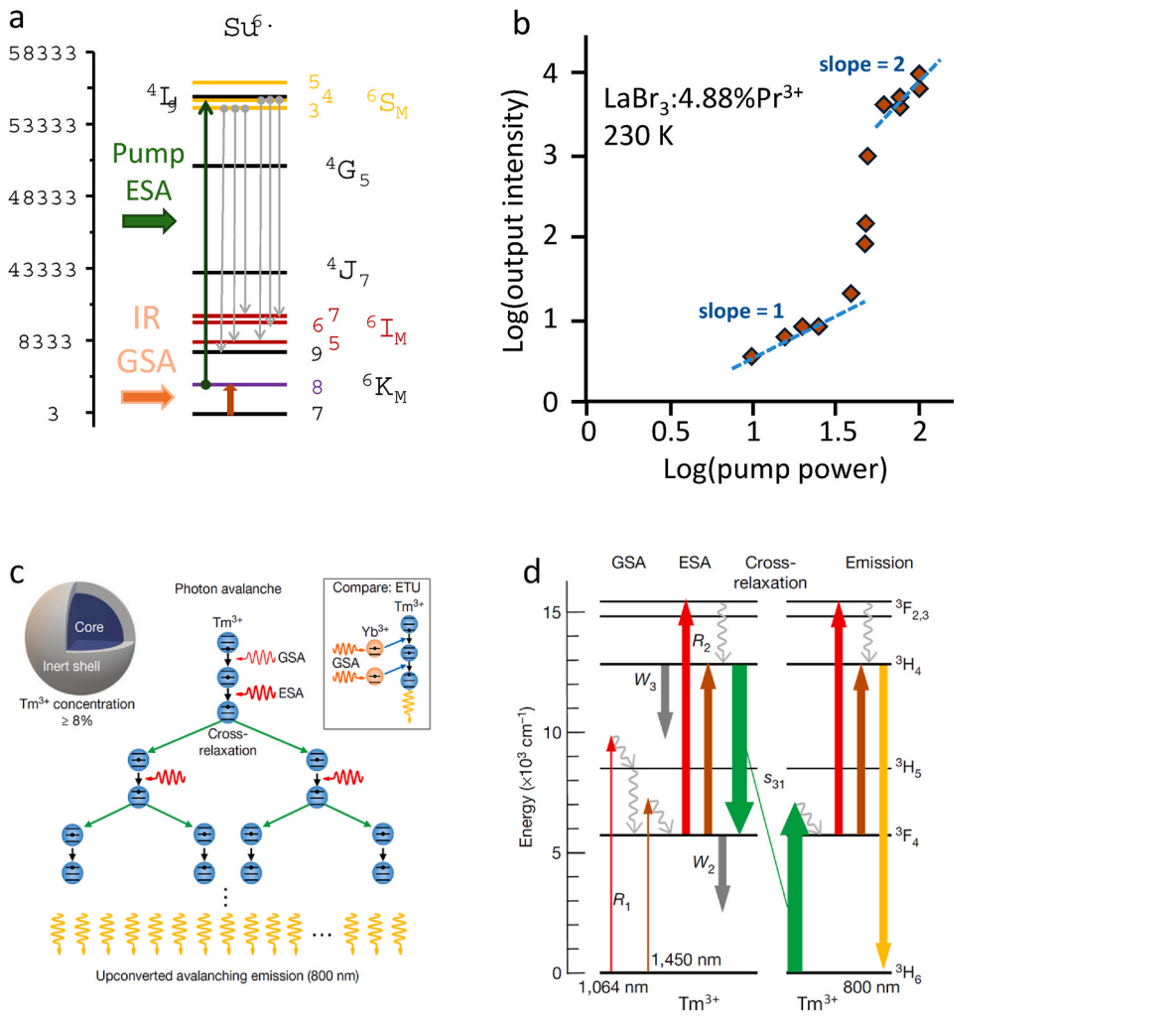

Fig. 11. a) Energy diagram for Pr^{3+} with GSA and ESA processes; b) Emission intensity versus pump power (log scales) for $LaBr_3$:4.88 % Pr^{3+} at 230 K; Redrawn from Ref. [64] © 1979 American Institute of Physics. c) Schematic of photon avalanche in $NaY_{1-x}Tm_xF_4$ UCNPs; d) Mechanism of photon avalanche; reproduced with permission from Ref. [65] © 2021 Nature Publ. group.

electric potential is reversed, luminescence is restored, and the process is reversible [71]. Electric-field modulation of lanthanide luminescence is not limited to purely inorganic materials; it is also feasible for coordination compounds, as for instance in cluster microparticles $\{Eu_{16}(\mu_4\text{-}F)_6(\mu_3\text{-}F)_{12}(^tBuCO_2)_{18}[N(CH_2CH_2O)]_4\}$ (EuFC-16). A small alternative electric potential (0–3 V) applied to single particles on a wide-field fluorescence microscopy imaging system fitted with an electrochemical cell and a spectroscope induces quenching of the Eu^{3+} luminescence; the latter recovers when the voltage decreases and the process is again perfectly reversible, yielding a time-modulation of the luminescence (Fig. 12a). Both quenching and recovery times are on the order of 0.8–1 s. The variation in luminescence intensity is due to a charging mechanism in that the microparticles located close to the electrode/electrolyte interface have a capacitor-like behavior under electrical potential that modifies their surface charge distribution; in turn the dielectric constant and the refractive index are modified, resulting in radiative lifetime and luminescence intensity changes [72].

Electric fields perturb the crystal field around Ln^{3+} ions leading to symmetry distortions that increase the radiative rates of f-f transitions. Another way of achieving CF distortion is to dope interstitial H^+ ions into the lattice of inorganic phosphors. This has been done for $NaMgF_3$:Yb^{3+},Er^{3+} in which the doped Ln^{3+} ions lie in a highly symmetrical octahedral site; H^+ induces a local charge distortion leading to anisotropic polarization of the F^- ligands and to the formation of F…H…F interactions that, *in fine*, alleviate the symmetry selection rules. The advantage of this procedure is that the lattice is subject to minimal distortion. An improvement of 3 orders of magnitude has been recorded for the Er^{3+} UCL intensity of the nanocrystals [73].

2.4.2. *Magnetic field modulation*

Luminescent lanthanide ions are paramagnetic so that they respond to external magnetic fields with great sensitivity. When submitted to a magnetic induction field, the CF electronic sub-levels are further split by the Zeeman effect, resulting in band shifting and intensity changes. Due to energy level shifts, cross relaxation and energy transfer processes are also affected. To take advantage of the effect of the magnetic field, heterostructures or glasses combining Ln-doped luminescent nanomaterials with magnetic materials have been designed that display strong responsiveness to magnetic fields [74,75]. A large body of works deals with the modulation of erbium luminescence by magnetic fields, either because of its use in erbium-doped fiber amplifiers (EDFAs) for telecommunications or in ubiquitous upconversion materials. Saurel et al. have demonstrated that in a nano glass-ceramic, the zero-phonon 1.5 μm emission of Er^{3+} shifts to higher energy and splits into a Zeeman doublet, enabling the flattening of the amplification band. The blue shift of the emission band has been ascribed to a quantum confinement effect [76]. Enhancing luminescence emission in $NaYF_4$:Yb(18 %),Er(2 %) UCNPs has been demonstrated for the first time in 2015 when P. Chen

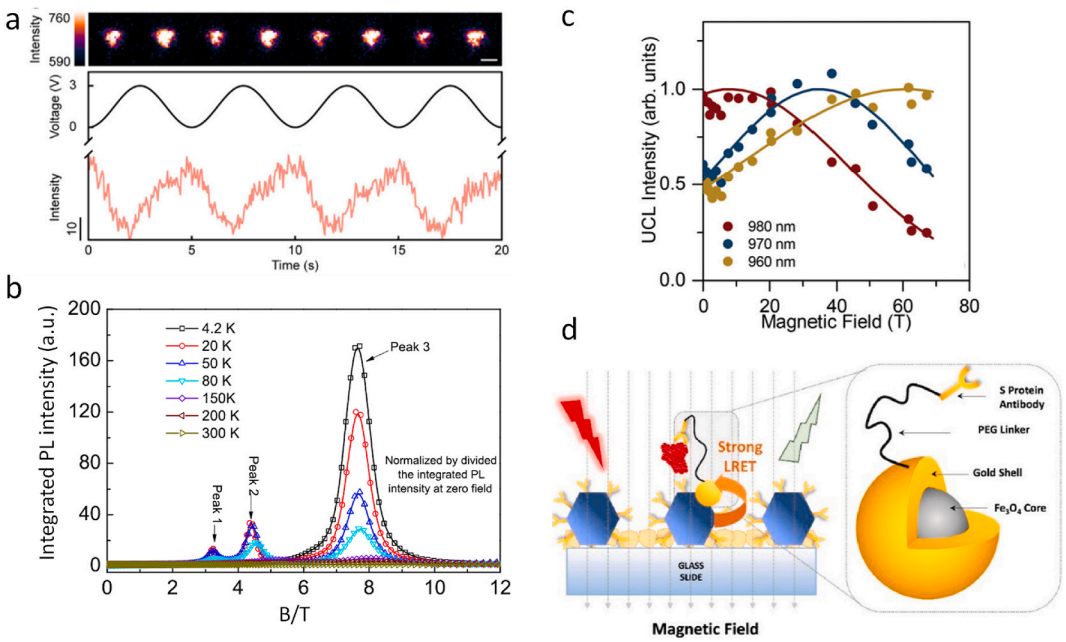

Fig. 12. a) Single EuFC-16 microparticle luminescence modulated by electric potential; scale bar: 1 μm. Reproduced with permission from Ref. [72] © American Chemical Society. b) Normalized integrated $^4S_{9/2}$ emission of a YVO_4:Er(2 %) single crystal *vs* pulsed magnetic induction field at different temperatures; reproduced with permission from Ref. [78] © 2015 AIP Publishing LLC. c) $Er^{3+}(^4S_{3/2} \rightarrow {}^4I_{15/2})$ UCL integrated intensity vs magnetic induction field *B* in function of excitation wavelength; reproduced with permission from Ref. [79] © 2020 The Royal Society of Chemistry. d) Principle of the UCL resonance energy transfer biosensor for the detection of the spike protein of Sars-CoV-2 virus; blue hexagons are the β-$NaGdF_4$:Yb,Er UCNPs decorated with the spike protein antibody, the red structure is the spike protein, the yellow forms on the plate represent bovine serum albumin (BSA) molecules added to prevent non-specific binding; reproduced with permission from Ref. [81] © 2024 The Royal Society of Chemistry.

et al. measured a 2.5-fold larger intensity of the red $^4F_{9/2} \rightarrow {}^4I_{13/2}$ emission by applying a 20 T field at 80 K [77]. The same year, a study of Er-doped (2 %) YVO_4 single crystals revealed that amplification of the $^4S_{3/2}$ and $^4I_{13/2}$ emissions occurs only for specific magnetic field ranges, centred at 3.2, 4.4, and 7.7 T, the latter leading to ~25-fold enhancement at 80 K (Fig. 12b). Interestingly, the depletion curve of the pump excitation Ar laser (488 nm) shows minima at the same fields, pointing to the enhancement essentially arising from enhanced absorption of light; a maximum 170-fold enhancement was reached for the green emission at 4.2 K and 7.7 T [78]. Not only can this phenomenon be used in the modulation of magneto-optical devices, but it can also be provided for the calibration of pulsed magnetic fields. The influence of magnetic-field on the luminescence of UCNPs has remained somewhat mysterious for several years, some authors observing a monotonic decrease with increasing magnetic induction field *B*, while others recorded an increase, as described above. Disparities in the reported results arise from different experimental conditions, particularly different excitation wavelengths. To resolve this problem, a comprehensive study has been conducted by Ł. Kłopotowski & coll. on β-NaYF4: Er^{3+},Yb^{3+} UCNPs under fields up to 70 T. The results clearly show that the magnetic field impact is similar for the luminescence intensity of both green and red emissions but depends on both the excitation wavelength and the strength of the magnetic induction field (Fig. 12c). The enhancement mechanism goes via a Zeeman-driven de-tuning between the excitation laser and the absorption transition, that is, via modification of the excitation efficiency as a result of Zeeman splitting; energy transfer efficiencies and multiphonon relaxation rates remain unaffected [79]. Presently, magnetic modulation of Ln^{3+} luminescence start to be used in various applications, for instance in the design of magneto-optic dual-signaled bar codes or in bioanalyses. The reported bar codes rely on magnetically-induced polarization. The activator is made up of hexanuclear molecular clusters $[Ln_6(teaH)_6(NO_3)_6]$ where $teaH^{2-}$ is doubly deprotonated triethanolamine. The spectral detection is somewhat involved, in that it implies magnetic circular dichroism (MCD) measurements, because of the intrinsic presence of MCD transitions in paramagnetic species eliminates the need to introduce chiral ligand for promoting polarization. Switching the direction of the magnetic field reverses the spectral signature, which adds an extra level of security to the barcodes [80]. An example of bioanalysis is the detection of the spike protein of the SARS-CoV-2 virus. The principle is illustrated in Fig. 12d. Hexagonal β-$NaGdF_4$:Yb(18 %),Er(2 %) UCNPs are fixed on a glass slide and then incubated with the spike protein antibody (SAb) that binds on their surface. In parallel, magnetic iron oxide Fe_3O_4 NPs are coated with a gold shell and linked to SAb by a long PEG chain (fully stretched length ~21.5 nm) yielding Fe_3O_4@Au-PeG-Sab (FAPS) that were added to the medium. The spike protein links to both SAb (on the UCNPs and FAPS) and when a magnetic field is applied (by simply using a small permanent magnet generating ~0.2 T), the Au-coated NPs are attracted downwards and enter into contact with the UCNPs, generating a strong LRET. With this protocol, the detection limit is reduced by a factor of 10 to 2.1 pg ml^{-1} [81].

2.5. Molecular and CPL upconversion

2.5.1. Molecular upconversion

The anti-Stokes process of upconversion where one or several lower energy photons are converted into higher energy ones, discovered already in the 1960s [82], has progressively taken importance in various materials and biomedical fields. In particular, the advent of nanoparticles and associated nanomaterials [83] has been instrumental in bringing new applications for UCL. The use of UCNPs in biomedical applications is justified by their easy derivatization and by the fact that biological tissues are more transparent to red (excitation) light. UCNPs are a perfect example of what scientists can do to overcome difficulties: at the beginning, the quantum yield (UCQY) of these nano objects was very low, on the order of 10^{-2}-10^{-4} % upon excitation power densities compatible with biological tissues. Waves of successive improvements, such as (i) the introduction of an inactive shell [84], learning from what

has been achieved with semiconducting and downshifting nanoparticles, (ii) a careful choice of the host material, and (iii) optimized synthetic methods [85], brought this number to around 10–15 %, and even to 40 % upon broad-band excitation (see above)! With the exceptions of organic molecules displaying triplet-triplet annihilation, a process that is analogous to upconversion, and a few attempts to generate upconversion in solution, UCNP materials and nanomaterials have usually purely inorganic matrices. It has long been thought that molecular upconversion in coordination compounds would not be possible because of the large number of phonons present in such molecular edifices. However, careful examination of the upconversion mechanism led to thinking that this difficulty can be overcome and in 2011 C. Piguet & coll. successfully demonstrated UCL in a Yb-Er-Yb trinuclear helicate dissolved in acetonitrile (Fig. 13a) [86]. Initially the mechanism was thought to mainly arise from a concerted energy transfer from Yb^{3+} to Er^{3+} (energy transfer upconversion, ETU): Cr($^2E \leftarrow {}^4A_2$) followed by Cr (^2E)-to-Er($^4I_{9/2}$) energy transfer (~50 % efficiency). However, subsequent studies of the Ga-Er-Ga trinuclear helicate with the same ligand and in the same solvent, demonstrated that excited state absorption in this compound (ESA) is quite efficient (UCQY = 1.7(2) × 10^{-9} at excitation power P = 25 Wcm^{-2}), because the Er($^4S_{3/2} \leftarrow {}^4I_{13/2}$) transition has a large molar absorption coefficient (ε = 43 ± 6 $M^{-1}cm^{-1}$) [87]. Therefore, careful analysis of all the energy transfer processes in the Cr-Er-Cr helicate (Fig. 13b), accompanied with theoretical simulation,

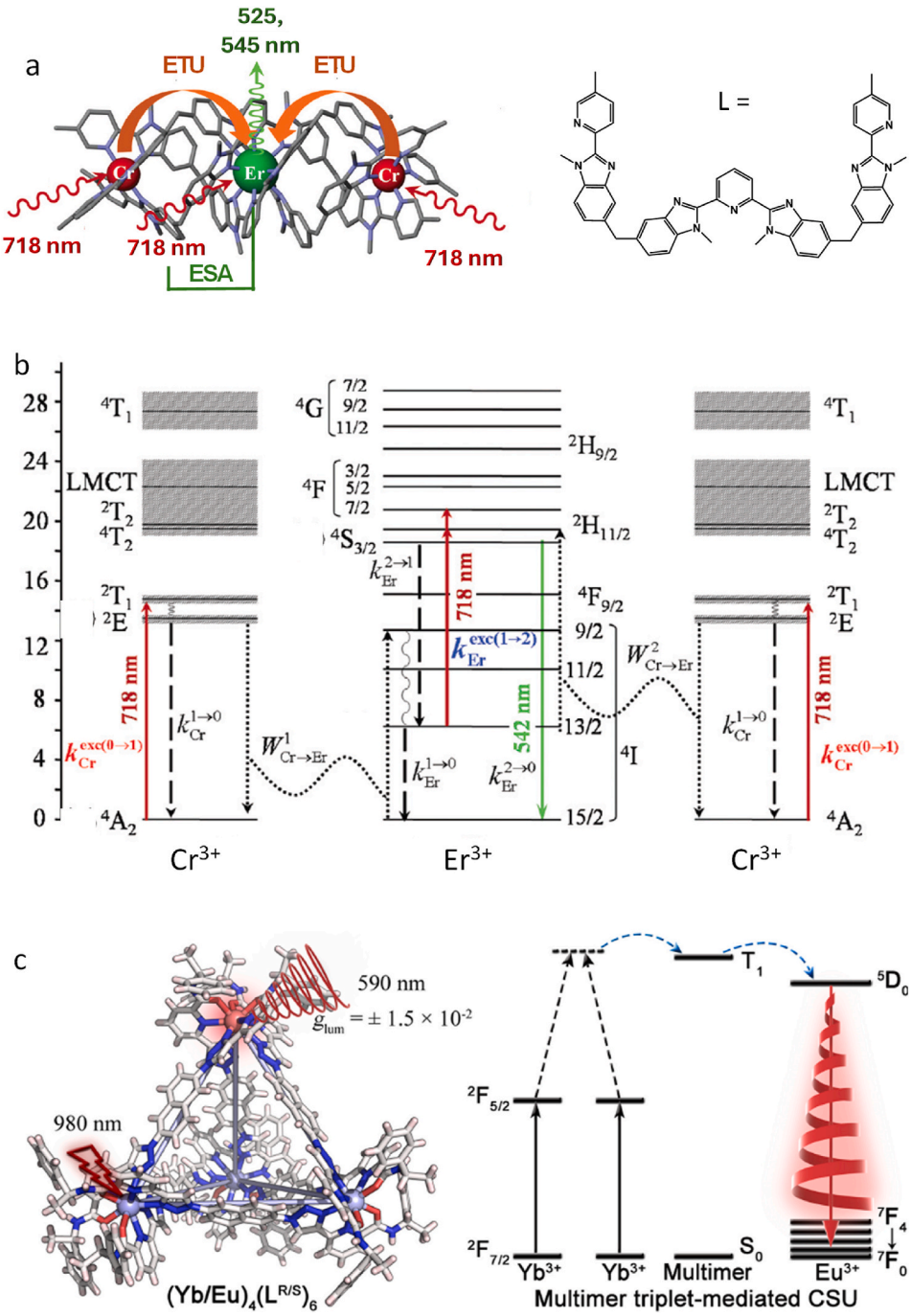

Fig. 13. a) Schematic representation of molecular upconversion in a Cr-Er-Cr helicate. b) Energy level scheme and main energy transfer paths. Adapted, with permission from Ref. [87] © 2021 The Royal Society of Chemistry. c) Upconverted CPL in an enantiopure tetrahedral cage, reproduced with permission from Ref. [96] © 2025 Chinese Chemical Society.

revealed that the simulated upconversion quantum yield based only on the ETU mechanism is 3–4 orders of magnitude smaller than the experimental quantum yield of 5.8×10^{-8} under 25 Wcm^{-2} excitation power; after introducing the ESA mechanism, the simulated evaluation grew closer to the experimental value. The conclusion is that both mechanisms are operative [87].

The demonstration that UCL can be generated in such large molecules is important for the biochemical community since UC "organic" bioprobes would certainly be welcome. One of the recurrent concerns of scientists involved in this fascinating new field is, however, the extremely low quantum yield. Advances are summarized in a recent review article [88] and latest data reported for Er^{3+} [89] are now showing UC quantum yields of $\sim 10^{-6}$ in solution, which is already a ~20-fold improvement with respect to the Cr-Er-Cr helicate. If the dynamics of improvement is like the one experienced for UCNPs, one can expect to reach UCQY of 0.1–1 % in a not-too-distant future, especially that the ESA mechanism is like the one exploited for photon avalanche (see above). In addition, broad-band excitation can also help boosting molecular UCQY: R. B. Cevallos-Toledo et al. have studied the photophysical properties of the mononuclear complex of Yb^{3+} with the deprotonated form of eosin and claimed that upon excitation into the Yb ($^2F_{5/2}$) level, an UCL band from eosin is seen at 600 nm with an estimated UCQY of 7.2×10^{-5} [90].

Other molecular architectures enable UCL from Tb^{3+} and Eu^{3+} ions and even observation of molecular UCL in deuterated water and water [88]. Polymetallic molecular clusters, coordination polymers, and metal-organic frameworks have also been used as substrates for molecular UCL of Eu^{3+} and Tb^{3+} [91]; a general overview of the various upconversion processes is given in Ref. [92].

Considering the latest development in molecular UCL, one can be reasonably optimistic that it will soon be added to the various lanthanide-based optical tools that biosciences are using. A first demonstration has been made with the bimetallic polynuclear complex $[Yb_5Tb_4(acac)_{16}(OD)_{10}](F_6\text{-TPB})$ where acac is acetylacetonate and F_6-TPB is perdeuterated 3,5-bis(trifluoromethyl)phenyl]borate. To overcome the very low UCQY, the authors have resorted to the classical but efficient technique of incorporating the luminescent probe into poly (ethyl-methacrylate) polymer nanoparticles with size ~40 nm: 1900 UC molecules could be incorporated per NP and well contrasted images of African green monkey kidney fibroblast-like COS7 living cells were obtained under 980-nm excitation and monitoring the green 540-nm channel [93].

2.5.2. Circularly polarized upconverted luminescence

Another important step further in molecular upconversion has been the demonstration of upconverted CPL. CPL is the active mechanism in several high-technology applications such as data storage, 3D-imaging, or optoelectronic devices. In order to shift the excitation wavelength in the NIR range, attention has focused on upconverted CPL (UC-CPL). Initially this has been achieved through triplet-triplet annihilation, 2-photon absorption, or interaction with UCNPs, as described in a 2024 mini review [94], but g_{lum} factors remained very small. Several ways have been tested to enhance this factor. P. Duan & coll [95]. have incorporated UCNPs and perovskite nanoparticles (PeNPs) into a chiral nematic liquid crystal (NLC). By positioning the emission peak of PeNPs in the middle of the photonic bandgap of NLC, enhanced UC-UCL is obtained thanks to radiative energy transfer UCNP-to-PeNP and g_{lum} reaches the large value of 1.1; moreover, an applied electric field can switch the upconverted emission from the UCNPs and, also, the radiative energy transfer process. Q.-F. Sun et al. have now brought the field a step further by assembling C_2-symmetrical ligands into heterometallic (Yb, Ln)$_4L_6^{R/S}$ tetrahedral cages (Ln = Eu, Sm), introducing a novel approach in the design of UC-CPL materials (Fig. 13c) [96]. In these edifices, UC-CPL is sensitized through the cooperative 980-nm absorption of two Yb^{3+} ions, reaching a virtual state in resonance with the ligand triplet state which, in turn, transfers energy onto the activator ion. The role of the triplet state is ascertained by the quenching of UC-CPL upon bubbling O_2 in the CD_3CN/MeOD solution. Mirror patterns were obtained in the UC-CPL spectra when L^S was substituted to L^R and the experimental g_{lum} factor reached 5.8×10^{-2} (592 nm) and 8.1×10^{-2} (565 nm) while the UCQYs were 1.9×10^{-7} and 1.4×10^{-8} for Ln = Eu and Sm, respectively.

2.6. Quantum bits

Two-level quantum systems can generate superposition states (quantum bits, qubits) that represent a formidable extension with respect to two-level electronic bits (*e.g.* 0,1), This property enables qubits to carry out multiple operations simultaneously, with exponential gains in computational speed over traditional computing methods. This fast-computing speed is crucial for quantum information processing (QIP) and led eventually to the development of quantum computers that reached the market in 2024. A simple representation of a qubit is given in Fig. 14a where the two "bit states" $|0\rangle$ and $|1\rangle$ are combined to generate a qubit state on Bloch's sphere, and can be written as [97]:

$$|\Psi\rangle = \cos\left(\frac{1}{2}\theta\right)|0\rangle + e^{i\varphi}\sin\left(\frac{1}{2}\theta\right)|1\rangle$$

If the qubit state is represented by a vector originating from the center of Bloch's sphere (with radius 1) the angles θ and φ are its spherical coordinates. Coherent oscillations between the two states $|0\rangle$ and $|1\rangle$ can be induced by a pulsed radiofrequency field resonant with the energy gap. The amplitude θ of the quantum superposition changes periodically at the Rabi frequency Ω_R, and so does the population $P_{|0\rangle}$. As time goes by, the oscillations are dampened in a decreasing exponential way characterized by time T_m (Fig. 1b) that is usually measured with pulsed-EPR spectroscopy. The potentiality of a system to be a good qubit is then evaluated by $Q = \Omega_R \times T_m$. that should be $> 10^4$-10^5, which often translates to $T_m > 100$ μs [98]. Although qubits can assume a large variety of states, the only states that can be identified with certainty are $|0\rangle$ and $|1\rangle$. Therefore, a major challenge is to be able to determine the final state with high probability. Qubits are central components of quantum information processing technologies, including quantum memories, quantum logic gates, photon entanglement, and quantum computing.

There are many ways of designing qubits, from using light, electrons, neutral atoms, trapped ions, superconducting circuits, to quantum dots, for instance; superposition of atomic and photonic states is also a way of getting qubits. Lanthanide atoms and ions are perfect candidates for qubits because of their strong magnetism, numerous electronic states and optical transitions, nuclear spin states, and because they are prone to generate long coherence times. Trivalent lanthanide ion doped into single crystals, silicon, or silicates are adequate materials for generating qubits [101]; for instance, a recent work has reported coherence times of nuclear spin states over 10 h in Y_2SiO_3:Eu^{3+} [102], opening large perspective for quantum information storage. This example also draw attention on the crucial role played by the hyperfine structure of the electronic configurations resulting from interaction with nuclear spin [97,99]. Useful trapped ions are Er^{3+}, Tm^+, and $^{171}Yb^+$; for instance, the latter, coupled with $^{138}Ba^+$ ions have generated 1-h coherence time qubits [100] (Fig. 14c). Finally, molecular qubits can be engineered from single-molecule magnets complexes such as terbium bis(porphyrinate),$TbPc_2$. In addition to long coherence times, the main advantages of lanthanide-based qubits lie in their optical addressability and strong interactions via magnetic dipoles.

A wealth of lanthanide coordination compounds are known that display single-molecule magnet properties, porphyrin sandwich complexes, polyoxometallates, organometallic compounds with cyclooctatetraene, to name but a few. These compounds have been evaluated with respect to their ability to generate qubits and quantum gates, and several of them were found to be adequate, such as double and triple

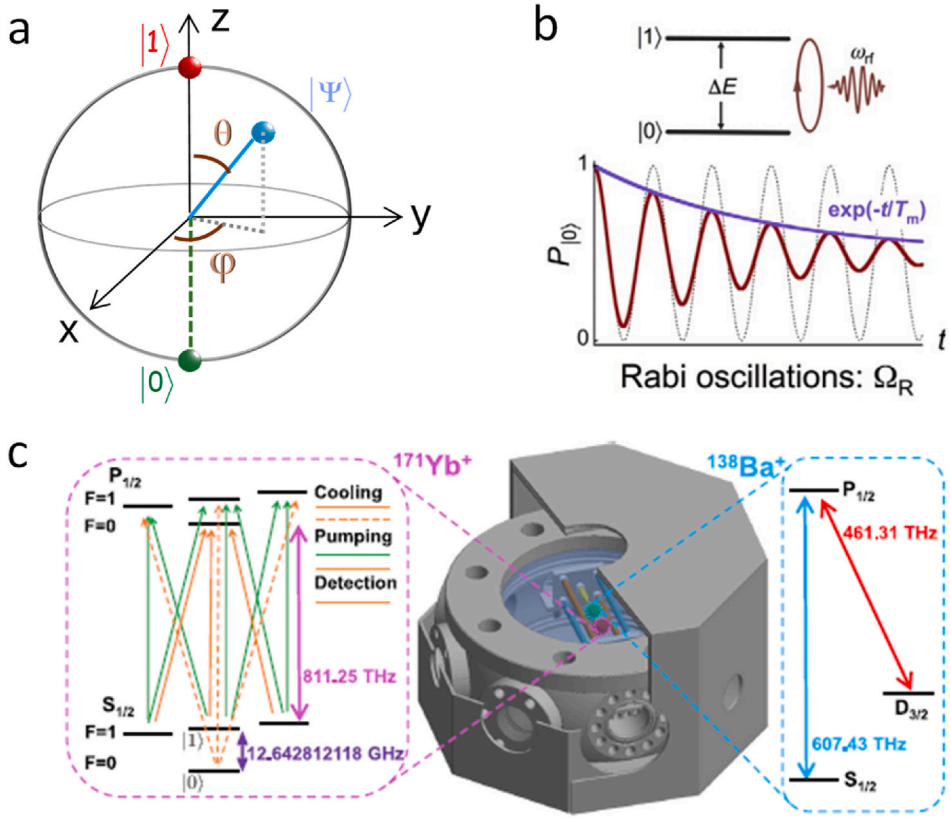

Fig. 14. a) Qubit state on Bloch's sphere as combination of two "bit states" $|0\rangle$ and $|1\rangle$. b) Population modulation and damping of state $|0\rangle$ under irradiation with a pulsed radiofrequency field; reproduced with permission from Ref. [99] © 2019 Elsevier B.V. c) Example of a set-up for generating long-coherence time qubits from the electronic levels of $^{171}Yb^{+}$ and $^{138}Ba^{+}$ ions; the octahedral chamber is protected by a μ-metal shielding with 10 holes, for connection of the vacuum pump and helical resonator and for accessing the laser beams, microwave, and imaging system; reproduced with permission from Ref. [100] © 2021, Nature Publishing Group.

decker complexes with porphyrins (*e.g.* $TbPc_2$ or Ln-Ln' heterometallic porphyrinates), metallo-azafullerene $Gd_2@C_{79}N$, or [Yb(trensal)] (trensal is 2,2′,2″-tris(salicylideneimino)triethylamine) [98]. The demanding characteristics of complexes able to generate qubits resulted in molecular chemists exploring less known Ln^{2+} coordination chemistry, for instance with Ln = La or Lu [103,104]. The largely forbidden nature of the $Eu^{3+}(^5D_0 \rightarrow {}^7F_0)$ emission line (Laporte's rule, spin rule, rules on ΔJ, ΔL) is of particular interest for QIP, as it is only weakly influenced by magnetic perturbations and is, therefore, known to exhibit fairly long optical coherence times. A spectral hole burning study, conducted on a pyrazole-phenanthroline nitrato complex, revealed a homogeneous linewidth of 1.55 MHz, corresponding to an optical coherence lifetime of 0.2 μs while the spin lifetime amounted to a stunning 41 s; these characteristics open perspective for the use of this complex in light-matter interfaces for QIP [105]. Following many examples from transition metal chemistry, the tunability of lanthanide-containing qubits has also been explored. In one study, the Gd^{3+} trigonal complex with trensal was chosen as a starting material because when compared with [Yb(trensal)], its phase memory time is 10 times larger (T_m = 2 μs) and coherence could be observed up to 125 K instead of 20 K for the Yb^{3+} analogue. In addition, Gd^{3+} has vanishing orbital momentum so that the sole influence of crystal-field splitting on the qubit behavior can be easily investigated by modifying the ligand. The outcome was that indeed, the Rabi frequency could be tuned and that small structural differences in the complexes can lead to large differences in CF-induced anisotropy [106]. Other recent efforts towards optimization of lanthanide-based qubits include the ^{171}Yb atom, described by three spin-1/2 constituents (2 electrons, and 1 nucleus with $I = ½$), which encompasses an optical qubit (*o*), as well as ground (*g*) and metastable (*m*) nuclear spin qubits. This *omg* architecture can be realistically controlled and coupled to Rydberg states for the generation of photon entanglement [107]. Other avenues in search of stable lanthanide-based qubits explore electric field control [108] or molecular qubits featuring metal-metal (*e.g.* Ca-Y) bonds [109].

3. Selected applications

The aim of this section is to draw attention to a handful of recent, sometimes less well-known but eye-catching, applications to underline how vivid lanthanide photonics is. We have chosen four particularly active fields, solid-state lighting, photovoltaics, mechanoluminescent probes, and biomedical applications. They are not systematically reviewed, and only short descriptions are given with a few typical references.

3.1. Solid-state lighting

Lighting is one of the daily applications that has most benefitted from lanthanide properties, from Auer mantle to fluorescent lamps and tubes with tricolor phosphors, to 1st generation of dc light-emitting diodes, to phosphor-converted ac LEDs. Altogether, referring to electric bulbs with tungsten filaments, rare earths have enabled 10-fold improvement on the electricity-to-light conversion efficiency, that presently reaches >90 %. Giving the large usage of lighting devices, it is understandable that scientists still try to not only improve the characteristics of phosphors but, also, to tailor them for specific applications. One of the tendencies is to try to mimic natural light as close as possible (Fig. 15a) [110] while simplifying the architecture of the phosphor materials. Henceforth the search for single-grain, full-visible spectrum white emitters, a recent example of which is $SrLiPO_4/Sr_9MgLi(PO_4)_7$:35 $\%Eu^{2+}$ that achieves 76 % internal quantum efficiency and 56 % external quantum efficiency with a high color rendering index of ~94 % [111].

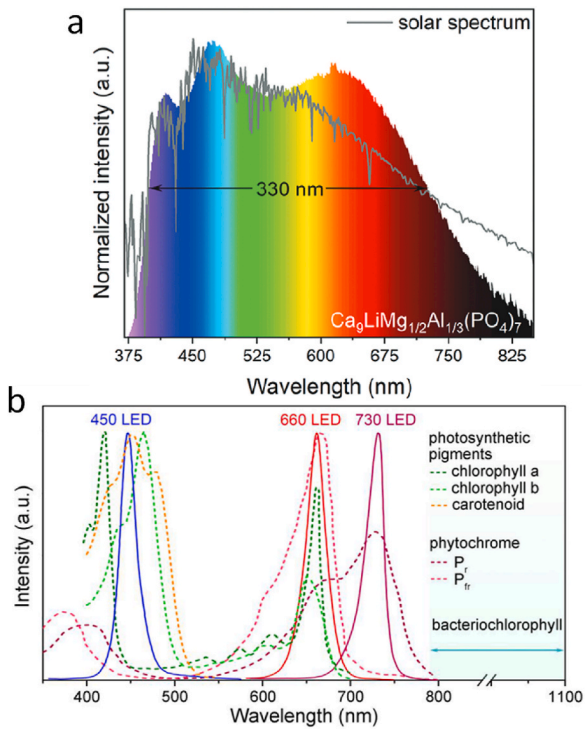

Fig. 15. a) Photoluminescence spectrum (λ_{ex} = 350 nm) of $Ca_9LiMg_{1/2}Al_{1/3}(PO_4)_7$:10 %$Eu^{2+}$ compared with sun emission; reproduced with permission from Ref. [110] © 2024 Wiley-VCH GmbH. b) Absorption spectra of plant growth pigments together with emission of relevant LED chips. Reproduced with permission from Ref. [112] © 2025 The Royal Chemical Society.

An important application is to provide light matching closely the absorption spectra of plant photoreceptors for greenhouses or indoor agriculture. Fig. 15b shows these spectra along with the emission spectra of some commonly used LEDs. The blue light in the 350–480 nm range promotes stem and leaf growth and corresponds mainly to absorption by chlorophylls and carotenoids. The 600–680 nm spectral range corresponds to absorption by chlorophylls and phytochromes and is responsible for flowering and fruit growth. These two absorption ranges represent >90 % of the energy indispensable to plant growth. Other spectral ranges are also useful, namely the 680–730 nm far red range corresponding to the light responses of the photosystems I (730 nm) and II (680 nm) and of the phytochromes. Less known and less studied to date is the absorption in the NIR 800–1100 nm range; this light is absorbed by photosynthetic bacteria involved in nitrogen fixation in plant roots and therefore also contributes to plant growth. The type of light needed for promoting plant growth largely depends on the geographical location of the plantations as well as on the immediate environment. In case of greenhouses, supplemental lighting is needed for high latitude areas and phosphor-converted LEDs (pc-LEDs) are commonly employed for specific complementary illumination in the blue and/or red/NIR spectral ranges. Indoor plant growth necessitates different lighting and full-spectrum lighting (sunlike) sources are the correct response. The phosphor materials corresponding to these two types of plant illuminations are detailed in C. Guo & coll. review [112].

While promoting plant growth by supplemental lighting is certainly safer than using fertilizers, the generated cost can be non-negligible. In case of greenhouses, an alternative action is simply to dope the plastic films with lanthanide wavelength-converting phosphors. As shown in Fig. 15b, plants have small absorptions in the ranges ~300–400 nm and ~500–580 nm, so that the idea is to convert these wavelengths into more useful ones for plant growth. Both lanthanide chelates and inorganic phosphors are used with activator ions such as Sm^{3+}, Eu^{2+}, Eu^{3+}, Tb^{3+}, or Dy^{3+}, sometimes allied with transition metal ions such as Ti^{4+}, Mn^{2+}, or Cu^{+}, for instance. A full description of these materials can be found in Ref. [113].

Another field of activity in which specific lighting is required is the marine environment [114]. Underwater acoustic and radio communications are often limited in their ability to simultaneously achieve high speed and long distance, so that visible light communication (VLC) emerges as a reliable alternative. Long transmission distances and adjustable bandwidth are advantages of VLC; in addition, the wavelength range between 380 and 780 nm is unlicensed, unlike radio frequencies, and its non-sensitivity to electromagnetic interferences add to the attractivity of VLC. Underwater wireless optical communication systems play now significant roles in tactical surveillance, pollution monitoring, climate change monitoring, offshore exploration, or remote vessel control. Laser LEDs are commonly employed as transmitter devices and new generations of lanthanide-containing pc-LEDs or micro-LED arrays are gaining importance. Light penetration in water depends on its wavelength and on the quality of water (Fig. 16). Light plays a vital role for marine organisms, their behavior being influenced by light intensity and photoperiods; the movement of fish in response to a light stimulus (phototaxis) consequently depends on the depth at which it is living; aquatic species in shallow water will better respond to red light, while deeper species will be more sensitive to blue-green light. This has consequences for seining and on the manipulation of commercially valuable species. More generally, the spectral preference of aquatic species impacts their optimal growth conditions so that versatile pc-LEDs offer the opportunity to tailor the lighting marine environment in aquaculture ranching systems. In addition to tuning pc-LEDs to the right wavelength, designers of these lighting systems have to take into account the inconvenience of marine environments, by designing moisture-resistant phosphors and/or tight encapsulation of the pc-LEDs [114].

3.2. Photovoltaics

The need for electricity keeps rising sharply in view of the increase in world population and of the implementation of a clean energy transition politics worldwide. In this context, solar energy stands out as the most abundant and one of the cleanest options available for renewable energy sources. Three generations of solar cells have been engineered. The first one is represented by silicon solar cells that are in common use today in view of their durability and reasonable efficiency (15–24 % for commercial panels); moreover, their price has been significantly reduced over the past decade and their lifespan reaches 30+ years. A second generation includes thin-film technologies (CdTe, CIGS = copper-indium-gallium-selenide) with efficiencies 22–24 %, but which face problems related to hazardous materials. The third generation is the most innovative one and encompasses dye-sensitized solar cells (DSSCs) [115], with conversion yields around 16 %, and more efficient perovskite solar cells (PeSCs), with yields reaching presently 21–25 %. These

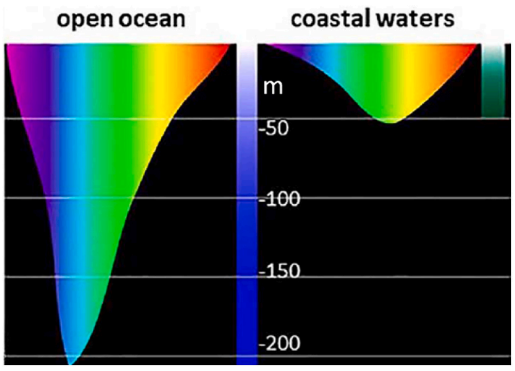

Fig. 16. Penetration depth of light into ocean waters in function of wavelength. Reproduced with permission from Ref. [114] © The Royal Society of Chemistry.

materials can be synthesized easily at low cost but have limited chemical stability, a problem that start to be addressed. The limited efficiency of solar cells stems from the fact that their absorption spectrum does not match sun emission well. Since the 1970s scientists came up with the idea of using lanthanides as wavelength-converting species in order to collect light not absorbed by the active material of the cell [116]. Two spectral ranges are of interest, 290–500 nm (~19 % of total solar output), and 1.2–2.5 μm (~17 %); the first one is useful for down-converting and downshifting materials and the second one for upconverting materials. Implementation is however not easy because it implies adding complexity to the fabrication of the solar panels, with limited benefits, a few more % on the conversion efficiency. Moreover, for upconversion layers, sunlight power density is too small for inducing strong signals, unless a concentrator is used, which, again, add to the complexity of the cell [117]. Nevertheless, researchers do not give up and a substantial amount of research focusses on DSSCs and PeSCs [118, 119] coupled with lanthanide wavelength converters. Regarding perovskite cells, their coupling with luminescent lanthanides can be achieved by simple mixing, chemical bonding, or nano printing (Fig. 17a and b). Both radiative (RET) and Förster (FRET) Ln-to-perovskite energy transfer processes have been identified, and the overall transfer can reach high values, even be quantitative [120]. Both perovskite NPs and UCNPs are highly modifiable, so that necessary fine tuning can be conveniently achieved; it is theoretically demonstrated that the maximum efficiency of UCNP-coupled PeSCs could reach 47 % for non-concentrated sunlight, substantially higher than the theoretical efficiency of the PeSCs alone (33 %) [121]. Fig. 17c displays the spectral ranges of the sun emission that can be harvested by various UCNPs and transformed into light absorbable by perovskites. The difficulty here is the low UC yield of UCNPs and low power density of sun emission. To overcome these hurdles, UCNPs have been coupled with dyes (see Section 2.3.2 above) and/or plasmonic gold thin films. A complex structure of IR-783 dye-sensitized $NaYF_4:Yb^{3+}/Er^{3+}@NaYF_4:Yb^{3+}/Nd^{3+}$ core-shell UCNPs coupled with plasmonic gold thin films led to 120-fold increment in UCL with the UCQY increasing from 0.2 % to 1.2 % under 8 Wcm^{-2} irradiation at 980 nm. When coupled to PeSC, the efficiency of the solar cell increased from 19.3 to 20.5 % and 21.1 % under 100 $mWcm^{-2}$ irradiation (1 AM 1.5G sun) and 1 Wcm^{-2} (concentrated 10 suns), respectively [122].

Producing electricity is one aspect, but storing it is another, more difficult one. This is one of the reasons why an energy economy based on hydrogen is being developed and tested. To remain green, hydrogen has to be produced with sun energy. Therefore, attention is attracted to photocatalysts for water splitting; among lanthanide catalysts, ceria is a valuable candidate since its bandgap (~2.7 eV) lies in the required range (>1.6 eV) for the production of an electron/hole pair [123]. Another application of ceria as photocatalyst is in the degradation of pollutants in wastewater [124].

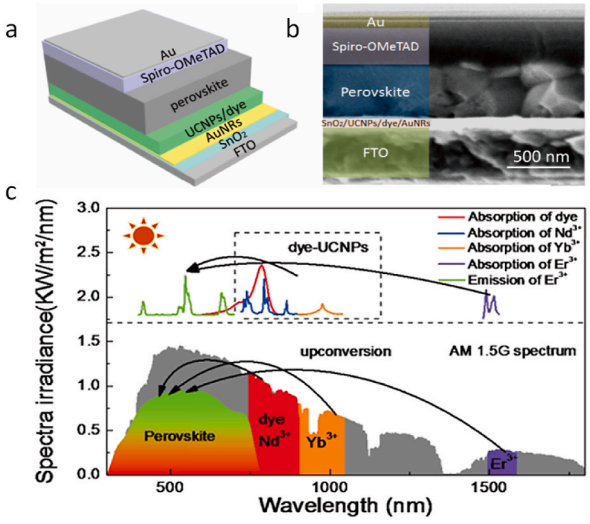

Fig. 17. a) Structure of a UCNP-coupled PeSC with b) its cross-sectional view. c) AM 1.5G sun emission spectrum showing fractions absorbed by PeSC and the spectral ranges that can be harvested by lanthanide-containing UCNPs with UCL from dye-Nd^{3+}, Yb^{3+}, and Er^{3+}. Reproduced with permission from Ref. [122] © 2020 American Chemical Society.

3.3. Mechanoluminescence

Mechanoluminescence (ML) is a long-known phenomenon whereby mechanical energy is transformed into light and that is extensively used in materials and structures testing and proofing. Many compounds, organic or inorganic, present this property and lanthanide-containing such materials are among the brightest known [125]; upconverted luminescence can also be triggered mechanically [126]. Characterization methods of ML have seen substantial improvements [127], and the field is now expanding to applications in anticounterfeiting, smart textiles, biosciences, and human-machine interfaces, attracting widespread research interest. Applications to materials [128] and to anticounterfeiting methods [129] are not presented here.

3.3.1. Self-recoverable mechanoluminescent materials

Emission from non-piezoelectric mechanoluminescent sensors is highly related to traps and thus they have to be charged prior use, that is, they have to be UV- or X-ray pre-irradiated for a short time (typically 5–20 min). The discovery of piezoelectric phosphors not necessitating pre-excitation is therefore a welcome step forward. Interesting materials in this respect are $Sr_3Al_2O_5Cl_2$:x%Ln (Ln = Ce^{3+} x = 4; Eu^{2+}, x = 6; Tb^{3+} x = 2) that were encapsulated into flexible polydimethylsiloxane polymer (PDMS). No pre-irradiation is required but pre-heating (in the range 25–350 °C) results in a small increase in ML intensity. Recovery time is about 1 h for 40 % of initial ML intensity, which can be shortened by heating at about 100 °C for 10 min (80 % recovery). The independence of the ML emitted by the elastomer samples from the intrinsic traps suggests that it involves direct excitation-emission processes within the Ln^{3+} energy levels. Several applications are proposed, including information storage and anti-counterfeiting [130]. Gallates are adequate hosts for green-emitting mechanoluminescent materials, for instance, $CaSrGa_4O_8$:xTb^{3+} [132] or the piezoelectric $Ca_5Ga_6O_{14}$:6 %Tb^{3+} phosphor featuring trap-independent and self-recoverable ML. The host structure is non-centrosymmetric and highly polar, resulting in large piezoelectricity; that is, upon mechanical stress, large piezoelectric charges are produced on the surface of the crystal, inducing an intense electric field that generates Tb^{3+} excited states. Interestingly, this material is perfectly self-recoverable, as shown in Fig. 18a [131].

A wealth of similar piezoelectric self-recoverable phosphors with various host matrices have been reported. Remarkably, nanoparticles can lead to the same phenomenon and, also, NIR emitting ML phosphors can be designed that are of interest as battery-free NIR light sources, *e.g.* for optoelectronics or biomedical engineering. Presently, pc-LEDs featuring Cr^{3+}-activated phosphors and excited by a blue chip are the main architectures for NIR light production. Therefore, building on this principle, F. Wang & coll [133]. have doped NPs of the large bandgap semiconductor β-Ga_2O_3 with Cr^{3+} ions occupying the octahedral sites. Further codoping with other ions, including RE^{3+} ions (RE = rare earth), introduces distortion of the octahedral geometry, enhancing the Cr^{3+} d-d transitions. The influence of the Ln^{3+} co-doping on Cr^{3+} ML intensity is shown in Fig. 18b. Crystal site engineering not only enhances the ML intensity but also shifts the emission maximum and influences the full-width-at-half-maximum (FWHM); a stunning example is shown on Fig. 18c where the 715-nm emission maximum of Ga_2O_3:1 %Cr^{3+},1 % Yb^{3+} is shifted to 830 nm upon further heavily doping with 40 % In^{3+} with concomitant broadening of the FWHM; in addition, the weak Yb^{3+} emission at ~1 μm is enhanced about 5-fold resulting in overall broad

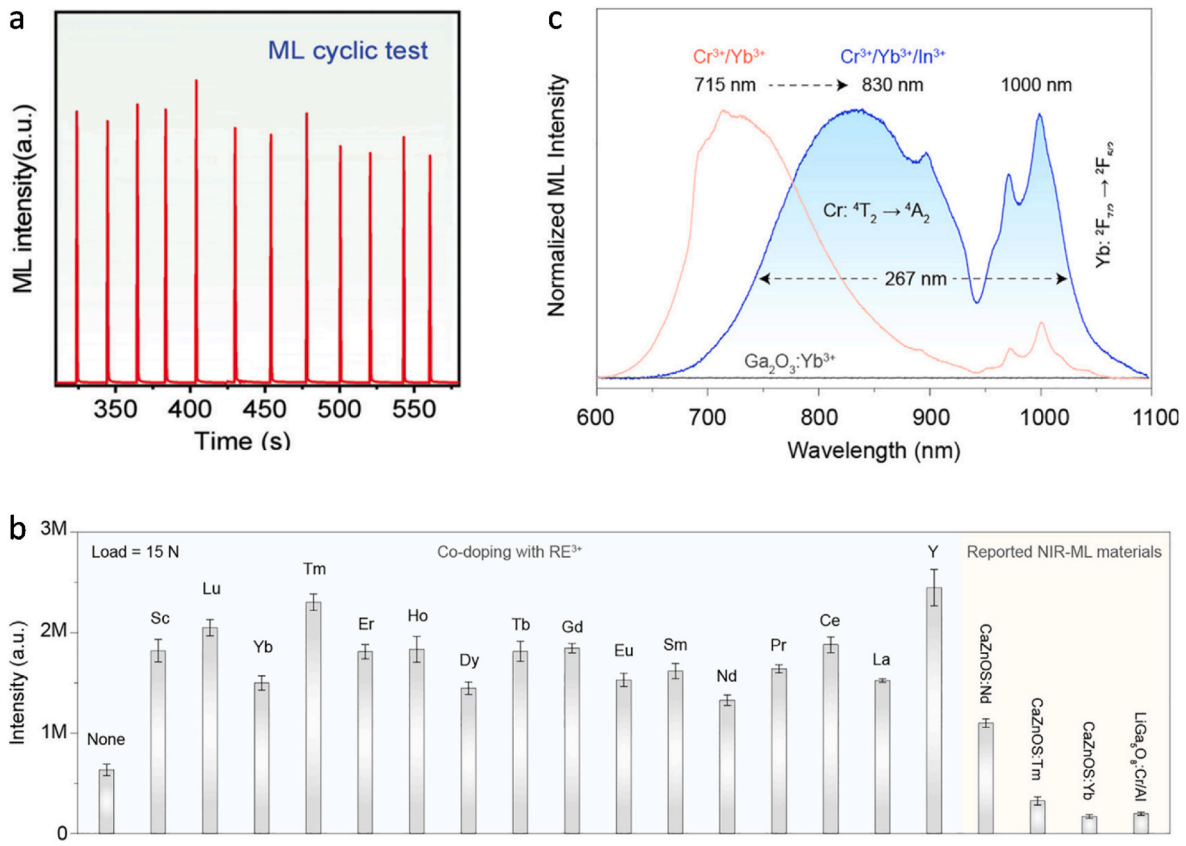

Fig. 18. a) Cycling test of the piezoelectric crystal $Ca_5Ga_6O_{14}$:6 %Tb^{3+} under constant impact force showing its large self-recoverability; reproduced with permission from Ref. [132] © 2022 The Royal Society of Chemistry. b) Normalized ML spectra of Ga_2O_3:1 %Cr^{3+}/1 %Yb^{3+} and Ga_2O_3:1 %Cr^{3+}/1 %Yb^{3+}/40 %In^{3+} (no ML signal was detected in Ga_2O_3:Yb^{3+}); c) effect of rare earth codoping in Ga_2O_3:1 %Cr^{3+}7 %RE^{3+} NPs on the ML intensity; reproduced with permission from Ref. [133] © 2023 Elsevier Inc.

NIR emission from 0.7 to 1.05 μm.

3.3.2. *Biological and medical sciences*

Mechanoluminescence starts to be used in biological living organisms because it can be excited by non-invasive techniques such as microwaves (300–3000 GHz) or ultrasonic waves (>20 kHz) that are well accepted in the medical community. Microwaves are used in some countries for cancer thermotherapy, while ultrasound is a universal medical imaging technique. Therefore, combining either of these techniques with mechanoluminescence can provide additional informative imaging or triggering of, for instance, photodynamic therapy. Moreover, arterial pressure, heart beats, or simply muscular movements generate mechanical forces that can excite mechanoluminescent sensors (heart beats have been detected with an organic ML sensor [134]).

Light does not penetrate deeply in biological tissues so that local light sources are sought for. In optogenetics, in which genetically modified cells are controlled by visible light, invasive implantation of tethered optical fibers is usually required. A way to avoid this insertion is to use mechanoluminescent nanoparticles acting as local light sources when triggered by brain-penetrating focused ultrasound (FUS), as demonstrated by X. Wu et al. with ZnS:Ag,Co@ZnS NPs emitting at 470 nm and that are delivered intravenously into blood circulation [135]. A remote regulation microdevice has been proposed as an alternative solution in another, anticancer, treatment. The idea is to achieve non-contact mechanical excitation of CaZnOS:3 %Tb^{3+} microcrystals. This phosphor was integrated into a magnetic regulation system made up of a free-moving magnet bar that triggers mechanoluminescence through the rotation motion set into action by an external magnetic field [136]. The emitted green ML then excites KillerRed, a genetically encoded red fluorescent protein that kills cancer cells by producing reactive oxygen species; the system was tested successfully on HeLa cells and on a subcutaneous tumor implanted into mice.

The cardiovascular and gastrointestinal systems rely on electric inductions of muscle activity to generate useful forces and to propel biomaterial. Dysfunction is this process causes motility diseases such as, for instance, food bolus transport in the esophagus, bladder function, or heart rhythms. Acquiring knowledge of the local pressure gradients generated by electric signaling is difficult in view of the lack of suitable non-invasive mechanosensors able to access neuromuscular cavities. To alleviate this situation, J. R. Casar et al. [137] have developed biocompatible micro gauges (MGs) made up of α-$NaYF_4$,18 %Yb^{3+},2 %Er^{3+}@$NaYF_4$ core-shell UCNPs embedded into polystyrene micro beads, and with approximate size of 1 μm. MGs are sensitive to uniaxial compressive forces in the range of a few μN. During compression the red-to-green ratio increases, then returns to its initial value upon the release of the acting force. The usefulness of the MG device is demonstrated on the luminal neuromuscular pharynx activity of live *Caenorhabditis elegans* (Fig. 19). Pharyngeal pumping is the animal's feeding method that produces a bite force on the order of 10 μN generating UCL for mechanical imaging. Embedding UCNPs into micro beads was needed in order for the MGs to bypass the filtering system of the pharynx that rejects particles smaller than 200 nm.

3.3.3. *Self-powered, wearable electronics and smart textiles*

Wearable electronics [138] and interactive (smart) fibers and textiles [139] are in the heart of a new, burgeoning industry that started about a decade ago. Understandably, cheap, classical ML materials such as zinc sulfide and derivatives were initially privileged, as well as ML organic molecules since they can more easily be incorporated into fabrics. Therefore, few works are presently available dealing with

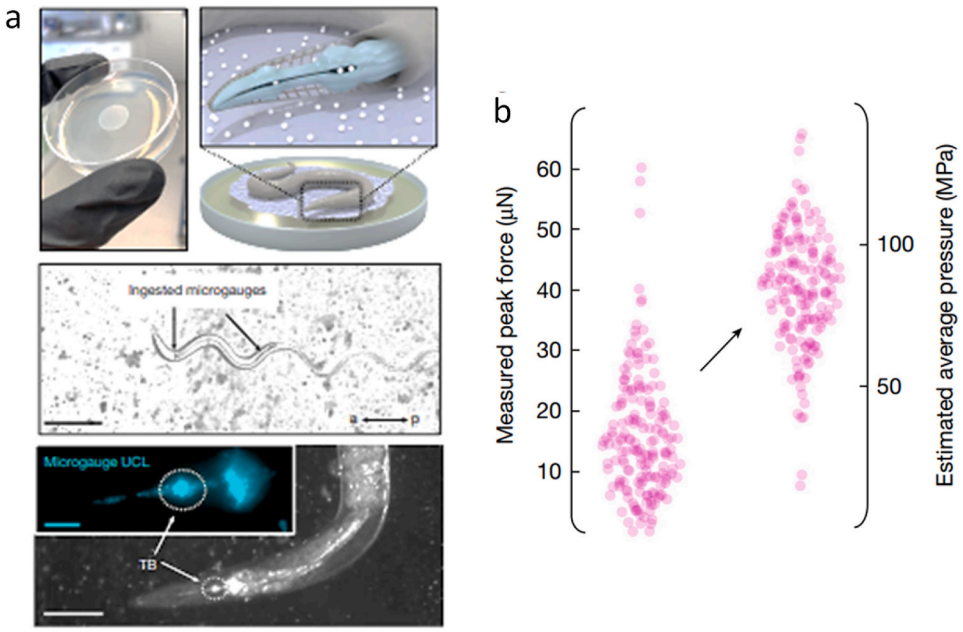

Fig. 19. a) Top: an agar plate and micro gauges lawn, a schematic representation of a *C. elegans* worm consuming micro gauges from this lawn and a pharynx highlighting the lumen-containing ingested micro gauges. Middle: an image of a worm on this lawn. Micro gauges (dark contrast) are visible in the upper and lower intestines. Bottom: false-colored UCL (cyan) and corresponding bright-field images from ingested micro gauges in the pharynx and upper intestine. Scale bars, 250 μm (top), 100 μm (bottom) and 20 μm (inset), TB is the tubular end. b), The maximum force change exhibited over each of the 169 measured events with a detectable increasing force (15.7 ± 10.1 μN, mean ± s.d.), as well as their corresponding average contact pressures (84 ± 20 MPa). Reproduced with permission from Ref. [137] © Nature Publishing Group.

lanthanide-containing ML phosphors. A flexible tactile sensing skin was obtained by codoping microparticles of the ubiquitous $SrAl_2O_4:Eu^{2+}$, Dy^{3+} inorganic ML material and of the temperature-sensing phosphor $Mg_4FGeO_6:Mn^{2+}$ into polyimide. Due to the dual nature of the composite, both temperature and stress signals are optically expressed, separated by different wavelengths. The sensing functions of this artificial skin were demonstrated and verified on a robot skin [140]. In another work, the same $SrAl_2O_4:Eu^{2+},Dy^{3+}$ ML material was fixed onto a layered graphene-based conductive cotton fabric and coated with polyurethane foam. The material is perfectly flexible, exhibits a controllable positive/negative electric response and its ML is intense and fully self-recoverable [141].

Human motion detection can be made by a PDMS elastomer including the $Gd_3Ga_5O_{12}:M$ (M = Eu^{3+}, Tb^{3+}, Bi^{3+}) multiple emitting phosphor. Multicolor ML from the device is triggered by contact electrification provoked by the interaction between the inorganic phosphor and PDMS under mechanical stress. It does not need pre-irradiation and is fully recoverable. Mechanical excitation can be from different sources, pressing, stretching, scratching, bending, tearing, and the elastomer can be processed into various threads and fabrics. An example of real-time dynamic stress sensing of human motion is given in Fig. 20a [142]. Hydrogels are other candidates of choice for such developments. They are highly stretchable (up to 9-fold) without disruption and when adequately tailored, can generate intense ML. This is the case of an interpenetrating polymer network made of poly(vinyl alcohol) (PVA) and poly(acrylic amide-co-2-acrylamido-2-methylpropane sulfonic acid) (PAMPS). Further introduction of glycine and Eu^{3+}, Tb^{3+} ions in this cross-linked network yields a highly sensitive sensor. The relative electric resistance change upon human motions is illustrated in Fig. 20b, while the ML luminescence was used for information encryption [143].

3.4. Biological and biomedical applications

Medicine and related bioanalytics are major and highly visible application areas for lanthanide luminescence (see preceding Section), encompassing clinical analyses, diagnostics with optical imaging techniques, and therapies such as photodynamic therapy of cancer or optogenetics. The number of papers published annually is very large and diverse so that we only describe a few works below, especially that the field has been covered by a recent review article [144].

3.4.1. Optical bioimaging

This aspect of lanthanide luminescence is regularly reviewed and depending on which organelle or tissue is to be imaged, a wealth of bioprobes have been proposed, such as simple chelates [146], metal-organic frameworks [145], peptide derivatives [147], to name but a few. Two areas are of particular interest. The first one is the advent of super-resolution luminescence microscopy (now termed nanoscopy) in which the classical Abbe's diffraction limit is overcome by a technique called super-resolution stimulated emission depletion (STED) microscopy. The luminophores are UCNPs in view of their bright and intense emission with single-particle sensitivity and the experimental setup requires a dual-laser confocal microscope. The STED mechanism for $NaYF_4$:18 %Yb^{3+},8 %Tm^{3+} is as follows: upon cw 980-nm excitation of Yb^{3+}, energy is transferred to the $^3H_4$ (2 photons), $^1G_4$ (3 photons), and $^1D_2$ (4 photons) excited electronic levels of Tm^{3+}. A second laser beam matching the $^3H_6$-$^3H_4$ energy gap (808 nm) triggers population inversion and stimulated emission from the $^3H_4$ level, preventing upconversion to the other levels. The 808-nm beam is spatially modulated to produce a doughnut shape that overlaps with the Gaussian form of the 980-nm excitation beam. Nanocrystals at the periphery of the 980-nm beam are switched off, leading to an excitation spot smaller than the diffraction limit. In these experiments, a resolution of 28 nm was achieved (1/36th of the excitation wavelength) [148]. The technique is especially useful for imaging single particles [149] and can be extended in the NIR spectral range by using downshifting NPs, with 808-nm excitation wavelength, 1064-nm depletion wavelength and emission between 850 and 900 nm. Lateral resolution narrows to 20 nm without photobleaching, under 19 kW cm^{-2} excitation power; these NPs also enable high-contrast tissue imaging with 70 nm resolution [150]. Optical multiplexing at the nanoscale shows promise for information encoding and a super-resolution multiplex imaging system based on

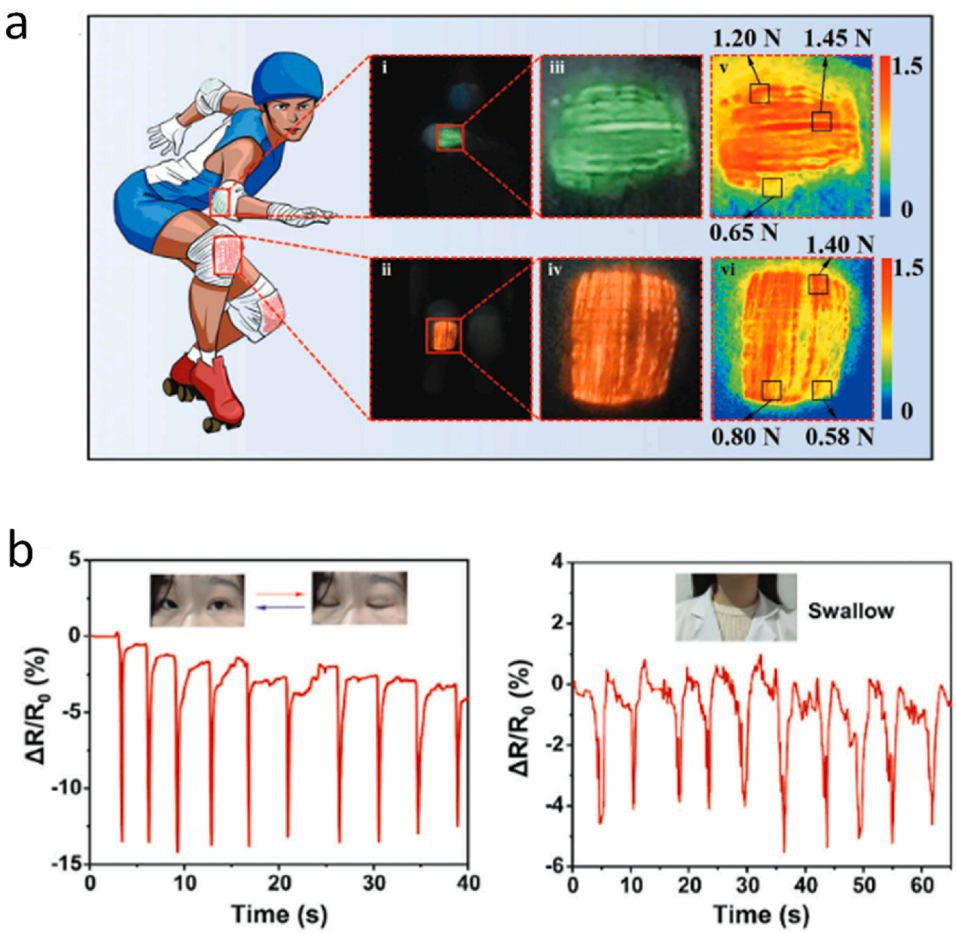

Fig. 20. a) Real-time stress distribution in elbow and knee as evidenced by ML from the $Gd_3Ga_5O_{12}$:M (M = Eu^{3+}, Tb^{3+}, Bi^{3+}) multicolor phosphor embedded in PDMS; reproduced with permission from Ref. [141] © 2025 Wiley-VCH GmbH b) Relative resistance changes of the PVA-PAMPS-Gly-Eu^{3+},Tb^{3+} hydrogel as a strain sensor for human motions: blinking and swallowing; reproduced with permission from Ref. [143] © 2025 Wiley-VCH GmbH.

lifetime-tailored UCNPs has been proposed in conjunction with a deep learning algorithm coordinating the images; a 3-channel set-up demonstrated decoding accuracy above 93 % for each channel [151]. Super-resolution imaging with UCNPs is an energy-intensive technology inducing potential photo-damages and the present trend is to work towards lowering the needed energy threshold; one obvious solution is to increase the brightness of the NPs, by reducing their size, engineering a passivation shell, and using broadband excitation or plasmonic enhancement techniques [152].

The second fast developing area is the shift to the second biological transparency window (NIR-II, 1000–1800 nm) in order to maximize light penetration, both for imaging and therapeutical purposes [153]. The ideal system encompasses a NIR-I (650–900 nm) excitation with emission in the NIR-II window. Er^{3+} and Yb^{3+} complexes with fluorinated tetrapyrroles or porphyrins capped with (ideally deuterated) Kläui's ligand are particularly efficient with quantum yield reaching 10-13 % in water for Yb^{3+} [154]. In a continuous effort to get away from tissue scattering and autofluorescence, F. Zhang & coll. have now designed $LiYF_4$:10 %Tm@$LiYF_4$: 70 %Er@$LiYF_4$ nanocrystals excitable at 1710 nm and emitting at 1650 nm. Compared to 1532-nm excited anti-Stokes probes, the signal-to-noise ratio improved 12.7-fold [155].

3.4.2. *Cancer diagnosis*

Micro RNAs (miRNAs) are short, non-coding, regulatory RNAs that emerged as valuable biomarkers for early cancer diagnosis [156]. Classical detection methods comprise Northern blotting, microarray technologies, and real-time quantitative reverse transcription polymerase chain reaction (qRT-PCR). While the first two have limited sensitivity, the last one is costly and lengthy. Therefore, bio-scientists try to develop new detection methods that are highly sensitive, cheap, and fast; in this context, lanthanide luminescent probes, particularly UCNPs, revealed to be tools of choice. For instance, miRNA-21 has been detected in MCF-7 and HeLa cells using a core@satellite probe. The core is made of magnetic NPs, obtained by doping Fe^{3+} into $Cu_{2-x}Se$ NPs and subsequently surface-decorated with DNA strands (DNA1). The satellite consists of $NaGdF_4$:Yb^{3+},Er^{3+} UCNPs surface-derivatized with other DNA strands (DNA2) complementary to DNA1. To render the probe soluble, UCNPs were further functionalized with PEG. Assembly of the probe is realized through interaction of the 2 DNA strands; on average, 14 UCNPs were attached to one core particle. As such, the probe is only weakly luminescent but upon interaction with miRNA-21, it dissociates. Not only is then full UCL restored, but the T_2 MRI signal is amplified, so that dual detection is feasible. The limit of detection reached was 5.8×10^{-21} mol/ng miRNA for luminescence detection and 18.2×10^{-21} mol/ng miRNA for the MRI signal [157]. A combination of enhancement techniques has been proposed for the detection of miRNA-373 with a $NaGdF_4$:Yb^{3+},Tm^{3+}@$NaGdF_4$:Yb^{3+},Nd^{3+} UCNP probe: catalytic hairpin assembly and activatable plasmon enhanced fluorescence with gold NPs coated with a silica shell. When irradiated at 808-nm, the UCNPs emits UCL at 365 and 460 nm that is absorbed by the activatable gold NPs emitting at 700 nm. Limit of detection reached 0.48 pM of miRNA-373. Furthermore, images of HeLa-tumor xenografted mice under 808-nm excitation clearly show the tumor site. It is noteworthy that direct irradiation into Yb^{3+} at 980-nm results in a temperature elevation from 30 to 60 °C, while 808-nm Nd^{3+} irradiation has negligible effect on temperature [158]; this is the reason why 808-nm excitation is now

preferred over 980 nm in biomedical research.

Clustered regularly interspaced short palindromic repeats (CRISPR) is an adaptative immune defense system found in most bacteria that is used as a gene-editing tool; when coupled with enzymes such as Cas9 or Cas12a, the system acts as molecular scissors enabling edits to genetic sequences. This feature is used in a dual assay of miRNA-155 and miRNA-let-7a which exhibit abnormal expression in breast cancer and are therefore promising markers for early detection. Microbeads are encoded with green- and blue-emitting core-shell-shell UCNPs ($NaYF_4$@$NaYF_4$:Yb^{3+},Ln^{3+}@$NaYF_4$, Ln = Er, Tm, respectively) with the help of 1-(3-dimethyl-aminopropyl)-3-ethylcarbodiimide (EDC) and then treated with DNA reporter probes that couple to the UCNPs and quench their UCL. In parallel, the target miRNA is transformed into a DNA probe thanks to CrRNA (acting as a guide for the CRISPR-Cas12 system) and when the latter is added to the UCNP-bearing beads, the reporter probes are cleaved, therefore restoring the UCL. Limit of detection of 12×10^{-18} and 22×10^{-18} mol are obtained for miRNA-155 and miRNA-let-7a, respectively. Moreover, the two miRNAs can be extracted from cancerous MCF-7 (breast), A549 (lung), and non-cancerous epithelial MCF-10A cells with their determined concentrations matching the results of classical PCR analysis. The sensitivity of this method is such that miRNA-155 is detectable at the single cell level in MCF-7 and A549 [159].

Sensing of miRNA-21 has been performed with a NIR-II probe for the characterization of colorectal cancer (CRC) that overexpresses this miRNA. The CRC sensor, schematized on Fig. 21a, is built on $NaErF_4$@$NaYF_4$ NPs (ErNPs) emitting at 1550 nm upon excitation at 808 nm or 980 nm; the ErNPs are derivatized by alendronate acid (ADA) and 4-mercaptobenzoic acid (MBA) followed by a linker for grafting the Na^+-dependent DNAzyme locked with a miRNA-21 pairing short strand and the corresponding DNAzyme substrate conjugated to the organic IR820 dye. The substrate is a DNA-RNA chimeric nucleic acid strand made up of a scissile adenosine ribonucleotide and two DNA domains capable of binding the DNAzyme. UCL emitted under 808-nm excitation is regulated by the IR820 dye (that absorbs at 808 too) and the UCL intensity ratio $R = L_{808}/L_{980}$ is small. When miRNA-21 comes into contact with the probe, the DNAzyme is activated and the IR820 fluorophores are released, leading to an increase in R that can be correlated with the concentration of miRNA-21. A limit of detection of 1.26 pM is reached and the protocol achieves an early and accurate diagnosis 2 weeks ahead of *in vitro* histology [160]. Significant progress has been made in tailoring lanthanide-doped nanoparticle-based strategies for miRNA detection, but translating laboratory findings into clinical practices still remains challenging, which triggers innovative research [161].

Prostate cancer is the second most widespread male cancer worldwide. Various detection methods of either acid phosphatases (ACP) or prostate specific antigen (PSA) are at hand, including luminescence ones, relying on gradual variation of the luminescence signal with the marker concentration. A bimetallic Eu/Tb-MOF was constructed using 5-(4-(triazole-1-yl)phenyl)isophthalic acid as the building block; subsequent decoration with hydroxyflutamide, a curing drug, yielded a sensitive sensor for the detection of prostate specific antigen (PSA) in real conditions such as biological matrices. The luminescence ratio of Eu^{3+} and Tb^{3+} exhibited a linear relationship with the concentration of PSA even in ng mL^{-1} ranges, with the luminescence quenched by the strengthening of hydrogen bonding interactions between the MOF, hydroxyflutamide and PSA. Interaction between the MOF and PSA was furthered determined through the reduced luminescence decay owing to PSA disrupting the energy transfer between the densely packed Eu^{3+} and Tb^{3+} ions [162]. A β-diketonate-europium chelate was designed for the immunodetection of prostate cancer cells (DU145) by ligating the IgG antibody MIL38 with the ligand through a tetraethylene glycol linker to enhance its hydrophilicity. Highly sensitive, time-gated luminescence was observed in DU145 cells stained with the europium complex, thereby achieving direct labelling of prostate cancer cells [163]. A joint

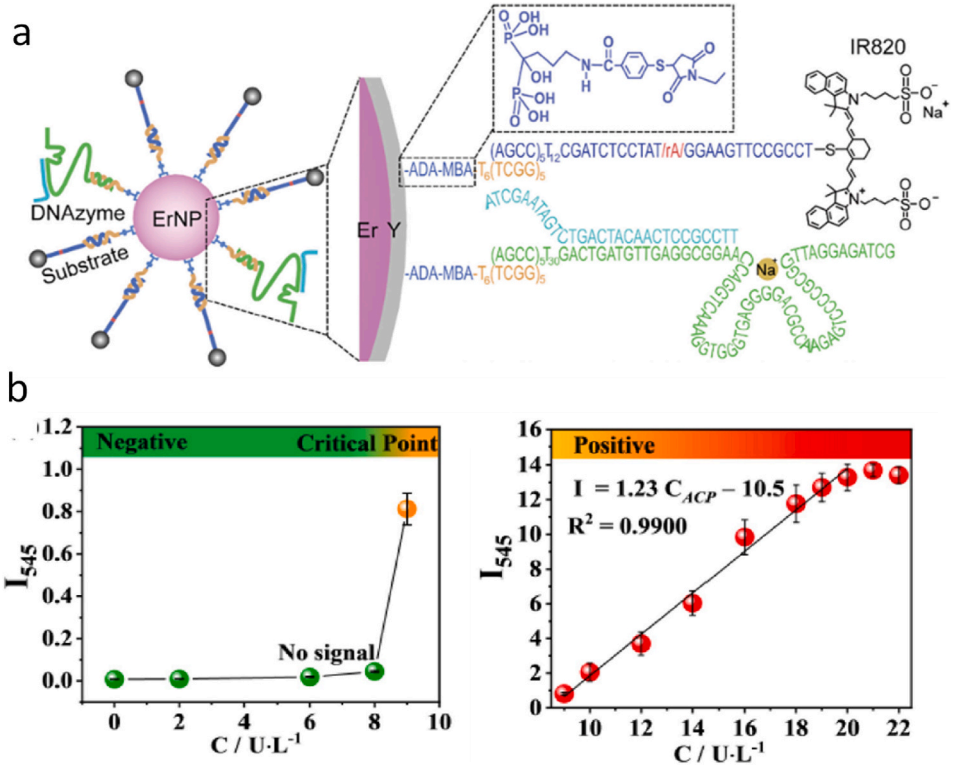

Fig. 21. a) Schematic illustration of the NIR-II colorectal cancer sensor; reproduced with permission from Ref. [160] © 2025 Wiley-VCH GmbH. b) Luminescence intensity changes of Tb-CeMOF at 545 nm with the increase of ACP concentration from 0 to 9 U L^{-1} (left) and 9–22 U L^{-1} (right); error bars indicate the standard deviations of three parallel experiments. Reproduced with permission from Ref. [166] © 2024 Wiley VCH GmbH.

study between Australian and Chinese research groups employed a similar strategy on upconversion nanoparticles, also using MIL39-biotinylated antibody to undergo ligand exchange to give highly specific immunodetection of DU145 cells [164]. Lengacher et al. designed a europium complex conjugated with prostate-specific membrane antigen that displayed targeted binding to PC-3 prostate cancer cells with a limit of detection as low as 1 nmol. Even though the luminescent complexes could be excited by two-photon excitation, they served as location beacons rather than analytical sensor [165].

However, there are often very small differences between normal and pathological states henceforth, the rates of false positive/negative diagnosis are high. To try overcoming this problem, a MOF-based sensor for acid phosphatases (ACPs) has been developed that shows a switch-on luminescence at the critical concentration at which pathology is most probable (9 U L^{-1}). The probe consists in a redox-active crystalline Ce^{IV} metal-organic framework (MOF) based on pyromellitic acid and Zr_6-BDC (benzenedicarboxylate) as linker; Tb^{3+} ions are subsequently bound to the Ce^{IV}-MOF through available carboxylate groups and L-ascorbic acid 2-phosphate trisodium (AAP) is added. The resulting Tb-Ce-MOF is non luminescent, and it remains in this dark state upon addition of ACP until the ACP concentration reaches 9 U L^{-1}, which triggers sudden Tb^{3+} emission (Fig. 21b). Above this concentration, the Tb^{3+} luminescence intensity increases linearly with the concentration of ACP. Absence of luminescence in the Tb-Ce-MOF arises from a low-lying ligand-to-Ce^{4+} charge transfer state deactivating the S_1 and/or T_1 ligand state(s), preventing antenna effect to Tb^{3+}. Addition of ACP catalyzes the transformation of AAP into ascorbic acid that subsequently reduces Ce^{4+}: XPS spectra show that upon addition of 9 U L^{-1} of ACP, the Ce^{3+} content increases from 46 % to 56 %, decreasing the influence of the LMCT state and restoring Tb^{3+} luminescence [166].

3.4.3. Photodynamic therapy

Light-controlled therapies have existed for more than 120 years. Present applications are often deployed in cancer therapies, ranging from photothermal therapy (PTT) to photodynamic therapy (PDT), light-controlled chemotherapy, and radiotherapy. Again, lanthanide-doped nanoparticles are at the forefront of the field because of their excitation and emission versatility – from NIR to X-rays, excellent photostability, and easy modification [167]. Lanthanide chelates also offer interesting perspectives. For instance, monoporphyrinate complexes of Gd^{3+} capped with Kläui's ligand and conjugated to peptides targeted towards $\alpha_v\beta$-integrin showed an impressive therapeutic index while enhancing *in vivo* MRI images [168].

PDT is a burgeoning field and is often combined with bioimaging [169] in what is termed theranostics, or with other therapies but, similarly to bioimaging, the present tendency is to move towards NIR excitation in order to increase the penetration depth, a factor limiting PDT to superficial cancers only [170]. Another way is to use deep-penetrating excitation waves well-accepted by the medical community, such as ultrasounds or X-rays [171], or even to dwell into the energy released by radionuclides during radiotherapy [172,173]. The combination between radiotherapy and PDT (X-PDT) is very interesting since it can reduce considerably the X-ray dose for the same therapeutical outcome. In one example, Tb^{3+} was reacted with rose Bengal (RB) in a solvothermal reactor to produce ~7-nm NPs that generated singlet oxygen and hydroxyl radicals under mild RX irradiation. Compared with bare RB, the amount of ROS was increased ~8 times. Upon internalization of Tb-RB NPs into luciferase-expressing murine epithelial breast cancer cells (4T1-luc), X-ray irradiation (0.5 Gy) resulted in an 50 % increase of cell death, compared to the effect of free RB [174]. For hypoxic cancers, PDT is difficult to use since there is not enough oxygen to generate $^1O_2$ and other ROS. Therefore, the same authors proposed a more sophisticated protocol in which Eu-doped $NaYF_4$ scintillator NPs are loaded with protoporphyrin IX as sensitizer, and an iron-containing porphyrin, hemin, as catalyst for oxygen generation from H_2O_2 present in the cells. Then the *in situ* produced $^3O_2$ can be converted into $^1O_2$ by the photosensitizer that absorbs red light emitted by Eu^{3+} under X-ray excitation. In this way, hypoxic cancer cells display the same death rate than normoxic cells [175].

While these new techniques are developing, X-ray treatment of cancer remains a major therapy and has also seen significant improvements, notably thanks to the advent of highly efficient lanthanide-based nano-scintillators [176] while swallowable X-ray detectors enable *in situ* quantification of the received dose [177].

3.5. Other applications

Almost any field in modern technology needs sensors and/or switches and light is an ideal transducer for these devices, since it can trigger or activate them without contact and at distance. Along these lines, temperature emerges as one of the most crucial parameters in many processes, and particularly in biochemical reactions [178], so that its measurement, including during a catalysis reaction [179] has attracted a myriad of developments using lanthanide luminescent probes, inorganic or organic [180].

Other applications of lanthanide luminescent materials include visible [181] and NIR [182] lasers, anticounterfeiting tags [183], forensic investigations [184], personal UV dose monitoring [185], viscosity measurements [186], plastic waste sorting [187], light-driven micromotors [188] that can be used in therapy [189], passive daytime cooling glasses [190], and quantum information processing, for instance for ensuring secure telecommunications [191].

Among photonic lanthanides, ytterbium is special element. Its stable isotope 171 (14 % abundance) generates qubits for quantum computing operations (see section 2.5) that minimize errors during initialization and manipulation and surpass 99.99 % fidelity. Indeed, $^{171}Yb^+$ can be confined by a quadrupole ion trap to generate, at the single particle level, a quantum phase transition [192]; moreover, $^{171}Yb^+$ ions in an interacting spin chain break spatial translational symmetry which leads to the new phase of matter dubbed "time crystal" [193]. In addition, inorganic matrices such as YAG, or glasses doped with ytterbium are used in laser cooling [194]. Lanthanide ions have equilibrium bond lengths in the ground and excited states that are very similar (leading to very small Stokes' shifts); their electric dipole forbidden transitions have minimal involvement of vibrational modes, thereby causing only small internal heating. This feature allows anti-Stokes emission to dominate in special cases. Lanthanide ions such as Dy^{3+}, Ho^{3+}, Tm^{3+}, Er^{3+}, and Yb^{3+} have energy levels relevant to laser cooling and Fig. 22 explains how thermal energy can be removed from an Yb^{3+}-doped material with a laser tuned on a specific m_J-$m_{J'}$ transition. Materials for optical refrigeration must be of highest purity and have low energy phonons, which hampers their development [195].

4. A bright future

The description of lanthanide photonics and its applications described above speak for itself: the field is burgeoning and attracts more and more enthusiastic people from many different horizons. From quantum physics to health care, clinical surgery, and green technologies,

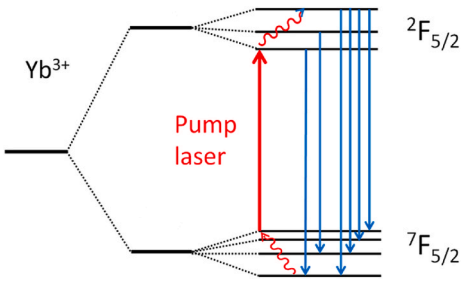

Fig. 22. Principle of laser cooling with Yb^{3+} ions. Redrawn from Ref. [194].

f-f luminescence is the motor of innovation and opens perspectives unheard of [196]. Its future is promising, as recent research on f-f luminescence has driven significant advancement in our knowledge on electronic state manipulation and material development for targeted applications, including bionics [197] and NIR optoelectronics [198]. We envision emerging innovations to pave way for improved imaging and sensing capabilities and to open stunning perspectives in a myriad of applications – from quantum physics to health care, clinical surgery, and green technologies. We should also expect to have to deal with challenges, as our understanding depends on the quality of our fabrication and characterization techniques, and the availability of hardware equipment. We must remain stringent in the experimental process, be meticulous in analysis, and be thorough with validation and cross checking. On the bright side, riding on the wave of artificial intelligence should bring unprecedented benefits, especially that integrating neural networks and machine learning will simplify the search for materials tailored for specific applications. Moreover, this will provide fresh momentum for medical optical imaging and light-driven therapies, while unlocking the full potential of lanthanide photonics for next-generation technologies—ushering in a new '*siècle des lumières*' (age of enlightenment)!

CRediT authorship contribution statement

Jean-Claude G. Bünzli: Writing – review & editing, Writing – original draft, Validation, Project administration, Data curation, Conceptualization. **Ka-Leung Wong:** Writing – review & editing, Validation, Formal analysis, Conceptualization.

Declaration of competing interest

The authors declare that they have no known competing financial interests or personal relationships that could have appeared to influence the work reported in this paper.

Acknowledgements

JCB aknowleges HongKong Polytechnic University for an adjunct professorship.

Data availability

No data was used for the research described in the article.

References

[1] R. Adunka, M.V. Orna, Carl Auer Von Welsbach: Chemist, Inventor, Entrepreneur, Springer Verlag, 2018.
[2] E. Baumgartner, Carl Auer Von Welsbach: a Pioneer in the Industrial Application of Rare Earths, in: C.H. Evans (Ed.), Episodes from the History of the Rare Earth Elements, Springer Netherlands, Dordrecht, 1996, pp. 113–129. Ch. 7.
[3] K. Binnemans, P.T. Jones, T. Müller, L. Yurramendi, Rare earths and the balance problem: how to deal with changing markets? J. Sustain. Metall. 4 (2018) 126–146.
[4] K.A. Gschneidner Jr., Industrial applications of rare Earth elements, in: ACS Symposium Series, vol. 164, American Chemical Society, Washington D.C., 1981.
[5] J.H. Van Vleck, The puzzle of rare-earth spectra in solids, J. Phys. Chem. 41 (1937) 67–80.
[6] J.-C.G. Bünzli, Discovery of the rare-earth elements, in: R. Pöttgen (Ed.), Rare Earth Chemistry, De Gruyter, Berlin & Boston, 2020, pp. 3–14. Ch. 1.1.
[7] J.-C.G. Bünzli, Lanthanide luminescence: from a mystery to rationalization, understanding, and applications, in: J.-C.G. Bünzli, V.K. Pecharsky (Eds.), Handbook on the Physics and Chemistry of Rare Earths, vol. 50, Elsevier Science, B.V., Amsterdam, 2016, pp. 141–176. Ch. 287.
[8] W.J. Evans, Tutorial on the role of cyclopentadienyl ligands in the discovery of molecular complexes of the rare-earth and actinide metals in new oxidation states, Organometallics 35 (2016) 3088–3100.
[9] Y.M. So, W.H. Leng, Recent advances in the coordination chemistry of cerium(IV) complexes, Coord. Chem. Rev. 340 (2017) 172–197.
[10] T.P. Gompa, A. Ramanathan, N.T. Rice, H.S. La Pierre, The chemical and physical properties of tetravalent lanthanides: pr, Nd, Tb, and Dy, structure, Dalton Trans. 49 (2020) 15945–15987.
[11] J.-C.G. Bünzli, Coordination compounds of lanthanides, in: R. Ameta, A.K. Rai, J. P. Bhatt, S. Bhardwaj, S.C. Ameta (Eds.), Photochemistry and Photophysics of Coordination Compounds. Fundamentals and Applications, vol. 1, Elsevier Inc., Amsterdam, 2023, pp. 341–389. Ch. 11.
[12] K. Ogasawara, S. Watanabe, H. Toyoshima, M.G. Brik, First-principles calculations of 4f-4f5d transition spectra, in: K.A. Gschneidner Jr, J.-C.G. Bünzli, V.K. Pecharsky (Eds.), Handbook on the Physics and Cemistry of Rare Earths Vol. 37, Ch. 231, 2007, pp. 1–59.
[13] P. Dorenbos, The 4f to 4f5d transitions of the trivalent lanthanides in halogenides and chalcogenides, J. Lumin. 91 (2000) 91–106.
[14] T. Kano, Principal phosphor materials and their optical properties: luminescence centers of rare-earth ions, in: S. Shionoya, W.M. Yen (Eds.), Phosphor Handbook, vol. 33431, CRC Press Inc., Boca Raton, FL, USA, 1999, pp. 177–200. Ch. 3.3.
[15] J.-C.G. Bünzli, A.-S. Chauvin, C.D.B. Vandevyver, B. Song, S. Comby, Lanthanide bimetallic helicates for *in vitro* imaging and sensing, Ann. N. Y. Acad. Sci. 1130 (2008) 97–105.
[16] V. Bachmann, C. Ronda, A. Meijerink, Temperature quenching of yellow Ce^{3+} luminescence in YAG:Ce, Chem. Mater. 21 (2009) 2077–2084.
[17] G.H. Dieke, H.M. Crosswhite, The spectra of the doubly and triply ionized rare earths, Appl. Opt. 2 (1963) 675–686.
[18] B.G. Wybourne, Spectroscopic Properties of Rare Earths, Wiley Interscience, 1965.
[19] W.T. Carnall, P.R. Fields, K. Rajnak, Electronic energy levels in the trivalent lanthanide Aquo ions I. Pr(III), Nd(III), Pm(III), Sm(III), Dy(III), Ho(III), Er(III) and Tm(III), J. Chem. Phys. 49 (1968) 4424–4442.
[20] W.T. Carnall, P.R. Fields, K. Rajnak, Electronic energy levels in the trivalent lanthanide Aquo ions II. Gd(III). Absorption spectra, J. Chem. Phys. 49 (1968) 4443–4446.
[21] W.T. Carnall, P.R. Fields, K. Rajnak, Electronic energy levels in the Trivalent lanthanide Aquo ions III Tb(III). Absorption spectra, J. Chem. Phys. 49 (1968) 4447–4449.
[22] W.T. Carnall, P.R. Fields, K. Rajnak, Electronic energy levels in the trivalent lanthanide aquo ions IV. Eu(III). Absorption spectra, J. Chem. Phys. 49 (1968) 4450–4455.
[23] B.R. Judd, Optical absorption intensities of rare Earth ions, Phys. Rev. 127 (1962) 750–761.
[24] G.S. Ofelt, Intensities of crystal spectra of rare Earth ions, J. Chem. Phys. 37 (1962) 511–520.
[25] B. Le Guennic, F. Riobé, F. Pointillart, Y. Suffren, K. Bernot, O. Cador, O. Maury, Deciphering crystal field splitting of lanthanide ions using magnetism, luminescence and ab-initio calculations: a friendly discussion between van Vleck and Boltzmann, in: J.-C.G. Bünzli, S. Kauzlarich (Eds.), Handbook on the Physics and Chemistry of Rare Earths, vol. 67, Elsevier B.V., 2025. Ch. 250, in press.
[26] M. Dolg, H. Stoll, H. Preuss, Energy-adjusted ab-initio pseudopotentials for the rare earth elements, J. Chem. Phys. 90 (1989) 1730–1734.
[27] M. Dolg, H. Stoll, A. Savin, H. Preuss, Energy-adjusted pseudopotentials for the rare earth elements, Theor. Chim. Acta 75 (1989) 173–194.
[28] M. Dolg, H. Stoll, H. Preuss, A combination of quasi-relativistic pseudopotential and ligand field calculations for lanthanoid compounds, Theor. Chim. Acta 85 (1993) 441, 340.
[29] S. Goedecker, M. Teter, J. Hutter, Separable dual-space Gaussian pseudopotentials, Phys. Rev. B 54 (1996) 1703–1710.
[30] J.B. Lu, X.L. Jiang, H.S. Hu, J. Li, Norm-conserving 4f-in-Core and basis sets pseudopotentials optimized for trivalent lanthanides (ln = Ce-Lu), J. Chem. Theor. Comput. 19 (2023) 82–89.
[31] M.G. Brik, C.G. Ma, Theoretical Spectroscopy of Transition Metal and Rare Earth Ions. from Free State to Crystal Field, Jenny Stanford Publishing Pte. Ltd., Singapore, 2020.
[32] B.M. Walsh, Judd ofelt theory: principles and practices, in: B. Di Bartolo, O. Forte (Eds.), Advances in Spectroscopy for Lasers and Sensing, Springer Verlag, 2006, pp. 403–433.
[33] P.R. Nawrocki, N. Kofod, M. Juelsholt, K.M.O. Jensen, T.S. Sørensen, The effect of weighted averages when determining the speciation and structure-property relationships of europium(III) dipicolinate complexes, Phys. Chem. Chem. Phys. 22 (2020) 12794–12805.
[34] A. Ciric, S. Stojadinovic, M. Sekulic, M.D. Dramicanin, JOES: an application software for Judd-Ofelt analysis from Eu^{3+} emission spectra, J. Lumin. 205 (2019) 351–356.
[35] R.T. Moura Jr., A.N. Carneiro Neto, E.C. Aguiar, C.V. Santos Jr., E.M. de Lima, W. M. Faustino, E.E.S. Teotonio, H.F. Brito, M.C.F.C. Felinto, R. A, S. Ferreira, L. D. Carlos, R.L. Longo, O.L. Malta, JOYSpectra: a web platform for luminescence of lanthanides, Opt. Mater. X 11 (2021) 100080.
[36] K.-L. Wong, J.-C.G. Bünzli, P.A. Tanner, Quantum yield and brightness, J. Lumin. 224 (2020) 117256.
[37] M.A. Crosby, R.E. Whan, R.M. Alire, Intramolecular energy transfer in rare Earth chelates. Role of the triplet State, J. Chem. Phys. 34 (1961) 743–748.
[38] M. Kleinermann, Energy migration in lanthanide chelates, J. Chem. Phys. 51 (1969) 2370–2381.
[39] S. Sato, M. Wada, Relations between intramolecular energy transfer efficiencies and triplet state energies in rare earths β-diketone chelates, Bull. Chem. Soc. Jpn. 43 (1970) 1955–1962.
[40] L.N. Puntus, K.A. Lyssenko, I. Pekareva, J.-C.G. Bünzli, Intermolecular interactions as actors in energy transfer processes in lanthanide complexes with 2,2'-Bipyridine, J. Phys. Chem. B 113 (2009) 9265–9277.

[41] G.F. de Sá, O.L. Malta, C. de Mello Donegá, A.M. Simas, R.L. Longo, P.A. Santa-Cruz, E.F. da Silva Jr., Spectroscopic properties and design of highly luminescent lanthanide coordination complexes, Coord. Chem. Rev. 196 (2000) 165–195.

[42] A.N. Carneiro Neto, E.E.S. Teotonio, G.F. de Sá, H.F. Brito, J. Legendziewicz, L. D. Carlos, M.C. Felinto, P. Gawryszewska, R.T. Moura, R.L. Longo, W.M. Faustino, O.L. Malta, in: J.-C.G. Bünzli, V.K. Pecharsky (Eds.), Modeling Intramolecular Energy Transfer in Lanthanide Chelates: a Critical Review and Recent Advances in *Handbook on the Physics and Chemistry of Rare Earths*, vol. 56, Elsevier B.V., Amsterdam, 2019, pp. 55–162. Ch. 310.

[43] J.D.L. Dutra, T.D. Bispo, R.O. Freire, LUMPAC lanthanide luminescence software: efficient and user friendly, J. Comput. Chem. 35 (2014) 772–775.

[44] P.A. Tanner, L. Zhou, C. Duan, K.-L. Wong, Misconceptions in electronic energy transfer: bridging the gap between chemistry and physics, Chem. Soc. Rev. 47 (2018) 5234–5265.

[45] L.F. Saraiva, A.N. Carneiro Neto, A.G. Bispo Jr., M.M. Quintano, E. Kraka, L. D. Carlos, S.A.M. Lima, A.M. Pires, R.T. Moura Jr., Role of vibronic coupling for the dynamics of intersystem crossing in Eu^{3+} complexes: an avenue for brighter compounds, J. Chem. Theor. Comput. 21 (2025) 3066–3076.

[46] Q. Zhang, L. Wu, X. Cao, X. Chen, W. Fang, M. Dolg, Energy resonance crossing controls the photoluminescence of Europium antenna probes, Angew. Chem. Int. Ed. 56 (2017) 7986–7990.

[47] L. Wu, Y. Fang, W. Zuo, J. Wang, J. Wang, S. Wang, Z. Cui, W. Fang, H.-L. Sun, Y. Li, X. Chen, Excited-state dynamics of crossing-controlled energy transfer in Europium complexes, J. Am. Chem. Soc. Au 2 (2022) 853–864.

[48] L. Wu, X.-D. Huang, W. Li, X. Cao, W.-H. Fang, L.-M. Zheng, M. Dolg, X. Chen, Lanthanide-dependent photochemical and photophysical properties of lanthanide−anthracene complexes: experimental and theoretical approaches, J. Am. Chem. Soc. Au 4 (2024) 3606–3618.

[49] P. Zhang, W. Steelant, M. Kumar, M. Scholfield, Versatile photosensitizers for photodynamic therapy at infrared excitation, J. Am. Chem. Soc. 129 (2007) 4526–4527.

[50] M.J.J. Mangnus, V.R.M. Benning, B. Baumgartner, P.T. Prins, T.P. van Swieten, A. J.H. Dekker, A. van Blaaderen, B.M. Weckhuysen, A. Meijerink, F.T. Rabouw, Probing nearby molecular vibrations with lanthanide-doped nanocrystals, Nanoscale 15 (2023) 16601.

[51] J.F. Suyver, J. Grimm, K.W. Krämer, H.U. Güdel, Highly efficient near-infrared to visible up-conversion process in $NaYF_4$: Er^{3+}, Yb^{3+}, J. Lumin. 114 (2005) 53–59.

[52] Y. Hu, Q. Shao, P. Zhang, Y. Dong, F. Fang, J. Jiang, Mechanistic investigations on the dramatic thermally induced luminescence enhancement in upconversion nanocrystals, J. Phys. Chem. C 122 (2018) 26142–26152.

[53] J. Zhou, S. Wen, J. Liao, C. Clarke, S.A. Tawfik, W. Ren, C. Mi, F. Wang, D. Jin, Activation of the surface dark-layer to enhance upconversion in a thermal field, Nat. Photonics 12 (2018) 154–158.

[54] C. Mi, J. Zhou, F. Wang, D. Jin, Thermally enhanced NIR–NIR anti-stokes emission in rare earth doped nanocrystals, Nanoscale 11 (2019) 12547.

[55] W. Zou, C. Visser, J.A. Maduro, M.S. Pshenichnikov, J.C. Hummelen, Broadband dye-sensitized upconversion of near-infrared light, Nat. Photonics 6 (2012) 560–564.

[56] G. Bao, S. Wen, G. Lin, J. Yuan, J. Lin, K.-L. Wong, J.-C.G. Bünzli, D. Jin, Learning from lanthanide complexes: the development of dye-lanthanide nanoparticles and their biomedical applications, Coord. Chem. Rev. 429 (2021) 213642.

[57] T. Tegafaw, Y. Liu, S.L. Ho, S. Liu, M.Y. Ahmad, A.K.A. Al Saidi, D. Zhao, D. Ahn, H. Nam, W.-S. Chae, S.-W. Nam, Y. Chang, G.H. Lee, High-Quantum-Yield ultrasmall Ln_2O_3 (Ln = Eu, Tb, or dy) nanoparticle colloids in aqueous media obtained via photosensitization, Langmuir 39 (2023) 15338–15342.

[58] X. Liu, T. Liu, Y. Feng, C.-J. Yao, Toward upconversion luminescence enhancement with dye sensitization, ACS Appl. Opt. Mater. 2 (2024) 1733–1750.

[59] M. Kaur, G.A. Mandl, S.L. Maurizio, G. Tessitore, J.A. Capobianco, On the photostability and luminescence of dye sensitized upconverting nanoparticles using modified IR820 dyes, Nanoscale Adv. 4 (2022) 608–618.

[60] M. Kaur, S.L. Maurizio, G.A. Mandl, J.A. Capobianco, Achieving photostability in dye-sensitized upconverting nanoparticles and their use in Fenton type photocatalysis, Nanoscale 15 (2023) 13583.

[61] T. Tegafaw, D. Zhao, Y. Liu, H. Yue, A.K.A. Al Saidi, A. Baek, J. Kim, Y. Chang, G. H. Lee, High quantum yields and biomedical fluorescent Imaging applications of photosensitized trivalent lanthanide ion-based nanoparticles, Int. J. Mol. Sci. 25 (2024) 11419.

[62] X. Cheng, J. Zhou, J. Yue, Y. Wsei, C. Gao, X. Xie, L. Huang, Recent development in sensitizers for lanthanide-doped upconversion luminescence, Chem. Rev. 122 (2022) 15998–16050.

[63] Q. Fan, C. Sun, B. Hu, Q. Wang, Recent advances of lanthanide nanomaterials in tumor NIR fluorescence detection and treatment, Mater. Today Bio 20 (2023) 100646.

[64] J.S. Chivian, W.E. Case, W.W. Eden, The photon avalanche: a new phenomenon in Pr^{3+}-based infrared quantum counters, Appl. Phys. Lett. 35 (1979) 124–125.

[65] C. Lee, E.Z. Xu, Y. Liu, A. Teitelboim, K. Yao, A. Fernandez-Bravo, A.M. Kotulska, S.H. Nam, Y.D. Suh, A. Bednarkiewicz, B.E. Cohen, E.M. Chan, P.J. Schuck, Giant nonlinear optical responses from photon-avalanching nanoparticles, Nature 589 (2021) 230–235.

[66] C. Liu, X. Zhang, X. Chen, L. Liang, Emerging advances in lanthanide photon avalanche nanophotonics, Nano Lett. 24 (2024) 15489–15500.

[67] C. Wang, Z. Wen, R. Pu, Q. Zhan, Giant optical nonlinear response up to 60^{th}-Order induced by the ytterbium energy relay mediated photon avalanches, Laser Photon. Rev. 18 (2024) 2400290.

[68] Y. Wang, J. Zhou, J. Gao, K. Zhang, C. Gao, X. Xie, L. Huang, Physical manipulation of lanthanide-activated photoluminescence, Ann. Phys. (Berlin) 531 (2019) 1900026.

[69] Y. Cai, G. Bai, S. Xu, J. Zhang, Rare earth ions feel the electric: a novel strategy to obtain efficient near-infrared photoluminescence, J. Alloys & Cmpds 768 (2018) 407–414.

[70] B. Su, Z. Wang, Y. Yang, C. He, Z. Deng, H. Chen, X. Long, In situ electric field tuning photoluminescence response in tetragonal-phase ferroelectric single crystals, ACS Appl. Electron. Mater. 2 (2020) 1729–1734.

[71] Y. Wang, J. Gao, C. Gao, H. Ma, B. Yang, Y. Han, E. Zhou, Q. Cheng, S. Jing, L. Huang, Modulation of lanthanide luminescence via an electric field, Nanoscale 11 (2019) 16562.

[72] W. Duan, Y. Yang, J. He, S. Lyu, Y. Chen, W. Zhu, S. Ling, C. Zhang, Y.-Z. Zheng, J. Feng, Electrically modulated fluorescence in single rare-earth particle, J. Phys. Chem. Lett. 16 (2025) 3185–3190.

[73] G. Li, S. Jiang, A. Liu, L. Ye, J. Ke, C. Liu, L. Chen, Y. Liu, M. Hong, Proof of crystal-field-perturbation-enhanced luminescence of lanthanide-doped nanocrystals through interstitial H^+ doping, Nat. Commun. 14 (2023) 5870.

[74] Y. Luo, Z. Chen, S. Wen, Q. Han, L. Fu, L. Yan, D. Jin, J.-C.G. Bünzli, G. Bao, Magnetic regulation of the luminescence of hybrid lanthanide-doped nanoparticles, Coord. Chem. Rev. 469 (2022) 214653.

[75] S.L. Zuo, P. Chen, C.F. Pan, Mechanism of magnetic field-modulated luminescence from lanthanide ions in inorganic crystal: a review, Rare Met. 39 (2020) 1113–1126.

[76] D. Saurel, V.K. Tikhomirov, V.V. Moshchalkov, C. Görller-Walrand, K. Driesen, Zeeman splitting and confinement effects in Er^{3+}-doped nano-glass-ceramics in magnetic fields up to 50 T, Appl. Phys. Lett. 92 (2008) 171101.

[77] P. Chen, H. Jia, Z. Zhong, J. Han, Q. Guo, J. Zhou, X. Liu, J. Qiu, Magnetic field modulated upconversion luminescence in $NaYF_4$:Yb,Er nanoparticles, J. Mater. Chem. C 3 (2015) 8794–8798.

[78] J. Zhang, X. Wang, Z. Zhong, Z. Ma, S. Wang, Y. Han, J.B. Han, L. Li, C. Tang, Magnetic field induced extraordinary photoluminescence enhancement in Er^{3+}: YVO_4 single crystal, A, Appl. Phys. 118 (2015) 083101.

[79] A. Borodziuk, M. Baranowski, T. Wojciechowski, R. Minikayev, B. Sikora, D. K. Maude, P. Plochocka, Ł. Kłopotowski, Excitation efficiency determines the upconversion luminescence intensity of β-$NaYF_4$:Er^{3+},Yb^{3+} nanoparticles in magnetic fields up to 70 T, Nanoscale 12 (2020) 20300.

[80] D.A. Gálico, M. Murugesu, Dual-signalled magneto-optical barcodes with lanthanide-based molecular cluster-aggregates, Nanoscale 15 (2023) 18198.

[81] J. Chen, W.K.H. Ho, B. Yin, Q. Zhang, C. Li, J. Yan, Y. Huang, J. Hao, C. Yi, Y. Zhang, S.H.D. Wong, M. Yang, Magnetic-responsive upconversion luminescence resonance energy transfer (LRET) biosensor for ultrasensitive detection of SARS-CoV-2 spike protein, Biosens. Bioelectron. 248 (2024) 115969.

[82] F. Auzel, History of upconversion discovery and its evolution, J. Lumin. 223 (2020) 116900.

[83] J. Zhou, J.L. Leaño Jr., Z. Liu, D. Jin, K.-L. Wong, R.S. Liu, J.-C.G. Bünzli, Impact of lanthanide nanomaterials on photonic devices and smart applications, Small 14 (2018) 1801882.

[84] G. Yi, G.M. Chow, Water-soluble $NaYF_4$:Yb,Er(Tm)/$NaYF_4$/polymer core/shell/shell nanoparticles with significant enhancement of upconversion fluorescence, Chem. Mater. 19 (2007) 341–343.

[85] C. Homann, N. Liu, H. Barbosa, E. Hemmer, Impact of synthesis routes on the optical performance of upconverting and near-infrared emitting lanthanide-doped nanoparticles, in: J.-C.G. Bünzli, S. Kauzlarich (Eds.), Handbook on the Physics and Chemistry of Rare Earths, vol. 65, Elsevier B.V., 2024, pp. 138–212. Ch. 340.

[86] L. Aboshyan-Sorgo, C. Besnard, P. Pattison, K.R. Kittilsved, A. Aebischer, J.-C. G. Bünzli, A. Hauser, C. Piguet, Molecular near-infrared to visible light upconversion in a trinuclear d-f-d complex, Angew. Chem. Int. Ed. 50 (2011) 4108–4112.

[87] B. Golesorkhi, I. Taarit, H. Bolvin, H. Nozary, J.-R. Jiménez, C. Besnard, L. Guénée, A. Fürstenberg, C. Piguet, Molecular light-upconversion: we have had a problem! when excited state absorption (ESA) overcomes energy transfer upconversion (ETU) in Cr(III)/Er(III) complexes, Dalton Trans. 50 (2021) 7955–7968.

[88] L.J. Charbonnière, A.M. Nonat, R.C. Knighton, L. Godec, Upconverting photons at the molecular scale with lanthanide complexes, Chem. Sci. 15 (2024) 3048–3059.

[89] S. Naseri, I. Taarit, H. Bolvin, J.-C.G. Bünzli, A. Fürstenberg, L. Guénée, G. Le-Hoang, M. Mirzakhani, H. Nozry, A. Rosspeintner, C. Piguet, Symmetry and rigidity for boosting erbium-based molecular light-upconversion in solution, Angew. Chem. Int. Ed. 62 (2023) e202314503.

[90] R.B. Cevallos-Toledo, D. Bellezza, J. Ferrera-González, A. Giussani, E. Orti, M. González-Béjar, J. Pérez-Prieto, Cooperative sensitization upconversion in Ytterbium(III)-Based eosin Lake pigments, ChemPhotChem 7 (2023) 1202300156.

[91] X.F. Duan, L.P. Zhou, H.R. Li, J.S. Hu, W. Zheng, X. Xu, R. Zhang, X. Chen, X. Guo, Q. Sun, Excited-Multimer mediated supramolecular upconversion on multicomponent lanthanide-organic assemblies, J. Am. Chem. Soc. 1435 (2023) 145 23121–23130.

[92] R. Sun, L. Sun, Rare-earth upconversion luminescence and its applications: from molecular to nano and micro scales, in: J.-C.G. Bünzli, S. Kauzlarich (Eds.), Handbook on the Physics and Chemistry of Rare Earths, vol. 65, Elsevier B.V., 2025, pp. 1–33. Ch. 337.

[93] L. Haye, F. Pini, L.K. Soro, R.C. Knighton, N. Fayad, M. Benard, F. Gagliazzo, M. E. Light, M.M. Natile, L.J. Charbonnière, N. Hildebrandt, A. Reisch, Molecular

upconversion nanoparticles for live-cell imaging, ACS Nano 19 (2025) 7178–7187.
[94] T. Zhao, P. Duan, Photon upconversion cooperates with downshifting in chiral systems: modulation, amplification, and applications of circularly polarized luminescence, Angew. Chem. Int. Ed. 63 (2024) 202406524.
[95] X. Yang, M. Zhou, Y. Wang, P. Duan, Electric-field-regulated energy transfer in chiral liquid crystals for enhancing upconverted circularly polarized luminescence through steering the photonic bandgap, Adv. Mater. 32 (2020) 000820.
[96] X.-F. Duan, H. Ji, L.-P. Zhou, S.-J. Hu, J. Fu, P. Duan, X.-Q. Guo, Q.-F. Sun, Upconverted circularly polarized luminescence on chiral lanthanide-organic tetrahedral complexes, CCS Chem. (2025), https://doi.org/10.31635/ccschem.024.202405005.
[97] P. Goldner, F. Alban, O. Guillot-Noël, Rare-earth doped crystal for quantum information processing, in: J.-C.G. Bünzli, V. Pecharsky (Eds.), Handbook on the Physics and Chemistry of Rare Earths, vol. 46, Elsevier B.V., 2015, pp. 1–78. Ch. 267.
[98] M. Atzori, R. Sessoli, The second quantum revolution: role and challenges of molecular chemistry, J. Am. Chem. Soc. 141 (2019) 11339–11352.
[99] G. Aromí, O. Roubeau, in: J.-C.G. Bünzli, V. Pecharsky (Eds.), Lanthanide Molecules for Spin-based Quantum Technologies in *Handbook on the Physics and Chemistry of Rare Earths*, vol. 56, Elsevier B.V., 2019, pp. 1–54. Ch. 309.
[100] P. Wang, C.Y. Luan, M. Qiao, M. Um, J. Zhang, Y. Wang, X. Yuan, M. Gu, J. Zhang, K. Kim, Single ion qubit with estimated coherence time exceeding one hour, Nat. Commun. 12 (2021) 233.
[101] W. Tittel, M. Afzelius, A. Kinos, L. Rippe, A. Walther, Quantum networks using rare-earths, quant, Sci. Technol. 10 (2025) 033002.
[102] F. Wang, M. Ren, W. Sun, M. Guo, M.J. Sellars, R.L. Ahlefeldt, J.G. Bartholomew, J. Yao, S. Liu, M. Zhong, Nuclear spins in a solid exceeding 10-Hour coherence time for ultra-long-term quantum storage, PRX Quantum 6 (2025) 010302.
[103] K. Kundu, J.R.K. White, S.A. Moehring, J.M. Yu, J.W. Ziller, F. Furche, W. J. Evans, S. Hill, A 9.2-GHz clock transition in a Lu(II) molecular spin qubit arising from a 3,467-MHz hyperfine interaction, Nat. Chem. 14 (2022) 392–397.
[104] R. Stewart, A.B. Canaj, S. Liu, E. Regincós Martí, A. Celmina, G. Nichol, H.-P. Cheng, M. Murrie, S. Hill, Engineering clock transitions in molecular lanthanide complexes, J. Am. Chem. Soc. 146 (2024) 11083–11094.
[105] S. Schlittenhardt, E. Vasilenko, V. Unni, N. Jobbitt, O. Fuhr, D. Hunger, M. Ruben, S.K. Kuppusamy, Spectral hole-burning studies of a mononuclear Eu(III) complex reveal narrow optical linewidths of the $^5D_0$-$^7F_0$ Transttion and Seconss Long luclenr Spin sifetlmes, ChemPhysChem 25 (2024) e202400280.
[106] S.H. Hansen, C.D. Buch, H. Weihe, S. Piligkos, Effect of chemical modification in trigonal Gd(III) molecular qubits, Inorg. Chem. 64 (2025) 4912–4919.
[107] N. Chen, L. Li, W. Huie, M. Zhao, I. Vetter, C.H. Greene, J.P. Covey, Analyzing the Rydberg-based omg architecture for ^{171}Yb nuclear spins, ArXiv 2201 (2022) 04083v1.
[108] W.T. Morrillo, H.I.J. Cumming, A. Mattioni, J.K. Staab, N.F. Chilton, Ab initio design of molecular qubits with electric field control, J. Am. Chem. Soc. 146 (2024) 25841–25851.
[109] J. Qiu, L. Abella, X. Du, Z. Cao, Z. He, Q. Meng, Y. Yan, J.M. Poblet, L. Sun, A. Rodríguez-Fortea, N. Chen, ScCaY@C2n: exploring molecular qubits with Ca-Y metal-metal bonds, J. Am. Chem. Soc. 146 (2024) 24310–24319.
[110] S. Liu, L. Li, X. Qin, R. Du, Y. Sun, S. Xie, J. Wang, M.S. Molokeev, S. Xi, J.-C. G. Bünzli, L. Zhou, M. Wu, Achieving ultra-broadband sunlight-like emission in single-phase phosphors: the interplay of structure and luminescence, Adv. Mater. 36 (2024) 2406164.
[111] S. Liu, X. Yang, R. Du, S. Rao, T. Xiao, L. Zhou, J.-C.G. Bünzli, M. Wu, Single-grain high-efficiency full-visible-spectrum white emitters, Angew. Chem. Int. Ed. 64 (2025) e202502100.
[112] J. Xiang, J. Chang, C. Chen, S. Jin, R. Chen, R. Gao, M. Jin, C. Guo, Recent progress of inorganic phosphors in artificial plant cultivation LEDs, J. Mater. Chem. C 12 (2025) 1538–1556.
[113] N. Zhang, Research progress of rare earth light conversion agent materials for agricultural film, Mater. Res. Express 11 (2024) 092001.
[114] M. Hua, S. Liu, L. Zhou, J.-C.G. Bünzli, M. Wu, Phosphor-converted light-emitting diodes in the marine environment: current status and future trends, Chem. Sci. 16 (2025) 2089–2104.
[115] H. Zhou, M. Md Aftabuzzaman, S.H. Kang, H.K. Kim, Key materials and fabrication strategies for high-performance dye-sensitized solar cells: comprehensive comparison and perspective, ACS Energy Lett. 10 (2025) 881–895.
[116] D.L. Dexter, Two ideas on energy transfer phenomena : Ion-pair effects involving the OH stretching mode and sensitization of photovoltaic cells, J. Lumin. 18 (1979) 779–784.
[117] J.-C.G. Bünzli, A.-S. Chauvin, in: J.-C.G. Bünzli, V.K. Pecharsky (Eds.), Lanthanides in Solar Energy Conversion in *Handbook on the Physics and Chemistry of Rare Earths*, vol. 44, Elsevier B.V., 2014, pp. 169–281. Ch. 261.
[118] Z. Li, B. Zhang, Z. Zhang, J.-C.G. Bünzli, A.R. bin Mohd Yusoff, Y.-Y. Noh, P. Gao, Vitamin needed: lanthanides in optoelectronic applications of metal halide perovskites, Mater. Sci. & Eng. R 152 (2023) 100710.
[119] G.A. Nowsherwan, M. Khan, N. Nowsherwan, S. Ikram, S.S. Hussain, S. Naseem, S. Riaz, Emerging trends in lanthanide-based upconversion and downconversion material for PSCs & DSSCs, J. Mater. Sci. 59 (2024) 16411–16448.
[120] W. Zheng, P. Huang, Z. Gong, D. Tu, J. Xu, Q. Zou, R. Li, W. You, J.-C.G. Bünzli, X. Chen, Near-infrared-triggered photon upconversion tuning in all-inorganic cesium lead halide perovskite quantum dots, Nat. Commun. 9 (2018) 3462.
[121] W. Zhang, W. Zheng, P. Huang, D. Yang, Z. Shao, X. Chen, The marriage of perovskite nanocrystals with lanthanide-doped upconversion nanoparticles for advanced optoelectronic applications, Aggregate 5 (2024) e558.
[122] W. Bi, Y. Wu, C. Chen, D. Zhou, Z. Song, D. Li, G. Chen, Q. Dai, Y. Zhu, H. Song, Dye sensitization and local surface plasmon resonance enhanced upconversion luminescence for efficient perovskite solar cells, ACS Appl. Mater. Interfaces 12 (2020) 24737–24746.
[123] P.K. Sahu, A. Champali, A. Prahan, B. Naik, Design, and development of nanostructured photocatalysts for large-scale solar green hydrogen generation, Sust, Energy Fuels 8 (2024) 1872–1917.
[124] J. Han, Q. Liu, H. Xu, Y. Wu, S. Le, C. Zhu, Cerium valence state conversion: fabrication and environmental remediation of modified CeO_2 materials, J. Rare Earths 43 (2025) 430–440.
[125] J.-C.G. Bünzli, K.-L.- Wong, Lanthanide mechanoluminescence, J. Rare Earths 36 (2018) 1–41.
[126] A. Lay, O.H. Sheppard, C. Siefe, C.A. McLellan, R.D. Mehlenbacher, S. Fischer, M. B. Goodman, J.A. Dionne, Optically robust and biocompatible mechanosensitive upconverting nanoparticles, ACS Cent. Sci. 5 (2019) 1211–1222.
[127] Y. Deng, D. Peng, S. Chang, J. Sun, J. He, C.X. Shan, L. Dong, Characterization methods for mechanoluminescent materials, J. Phys. D Appl. Phys. 58 (2025) 13002.
[128] Y. Zhuang, R.-J. Xie, Mechanoluminescence rebrightening the prospects of stress sensing: a review, Adv. Mater. 33 (2021) 2005925.
[129] T. Hu, F. Men, H. Yang, W. Lü, X.X. Han, G. Wang, Y. Gao, Q. Zeng, A self-recoverable mechano-photonic phosphor for high-level anti-counterfeiting, Mater. Today Chem. 44 (2025) 102553.
[130] Y. Bai, F. Wang, L. Zhang, D. Wang, Y. Liang, S. Yang, Z. Wang, Interfacial triboelectrification-modulated self-recoverable and thermally stable mechanoluminescence in mixed-anion compounds, Nano Energy 96 (2022) 107075.
[131] T. Hu, Y. Gao, B. Wang, T. Yu, D. Wen, Y. Cheng, Q. Zeng, A new class of battery-free, mechanically powered, piezoelectric $Ca_5Ga_6O_{14}$:Tb^{3+} phosphors with self-recoverable luminescence, J. Mater. Chem. C 10 (2022) 9554–9562.
[132] R. Shi, W. Liu, L. Li, H. Li, Z. Zhang, G. Rao, J. Zhao, Luminescence properties of a green-emitting mechanoluminescent phosphor $CaSrGa_4O_8$:xTb^{3+} without pre-excitation, RSC Adv. 14 (2024) 10726.
[133] H. Suo, Y. Wang, X. Zhang, W. Zheng, Y. Guo, L. Li, P. Li, Y. Yang, Z. Wang, F. Wang, A broadband near-infrared nanoemitter powered by mechanical action, Matter 6 (2023) 2935–2949.
[134] C. Wang, Y. Yu, Y. Yuan, C. Ren, Q. Liao, J. Wang, Z. Chai, Q. Li, Z. Li, Heartbeat-sensing mechanoluminescent device based on a quantitative relationship between pressure and emissive intensity, Matter 2 (2020) 181–193.
[135] X. Wu, X. Zhu, P. Chong, J. Liu, L.N. André, K.S. Ong, K. Brinson Jr., A.I. Mahdi, J. Li, L.E. Fenno, H. Wang, G. Hong, Sono-optogenetics facilitated by a circulation-delivered rechargeable light source for minimally invasive optogenetics, Proc. N. Y. Acad. Sci. 116 (2019) 26332–26342.
[136] Y. Zhang, X. Zhang, H. Wang, Y. Tian, H. Pan, L. Zhang, F. Wang, J. Chang, Remote regulation of optogenetic proteins by a magneto-luminescence microdevice, Adv. Funct. Mater. 21 (2021) 2006357.
[137] J.R. Casar, C.A. McLellan, C. Shi, A. Stiber, A. Lay, C. Siefe, A. Parakh, M. Gaerlan, X.W. Gu, M.B. Goodman, J.A. Dionne, Upconverting microgauges reveal intraluminal force dynamics in vivo, Nature 637 (2025) 76.
[138] W. Tang, Q. Sun, Z.L. Wang, Self-powered sensing in wearable electronics: a paradigm shift technology, Chem. Rev. 123 (2023) 12105–12134.
[139] H. Liu, Y. Shi, Z. Wang, B. Wang, Sensory interactive fibers and textiles, npj Flex. Electron. 9 (2025) 23.
[140] T. Cai, Y.-Z. Yan, J. Jung, J. Han, E. Yeom, Y. Im, T. Lee, D. Peng, Y. Liu, C.-S. Ha, K.C. Kim, Phosphorescence-based temperature and tactile multi-functional flexible sensing skin, Sens. Act. A Phys. 332 (2021) 113205.
[141] J. Liu, G.C. Lama, F. Recupido, C. Santillo, G. Gentile, G.G. Buonocore, L. Verdolotti, X. Zhang, M. Lavorgna, A multifunctional composite material with piezoresistivity and mechanoluminescence properties for a wearable sensor, Compos. Sci. Technol. 236 (2023) 109993.
[142] J. Wang, K. Yao, K. Cui, J. Zhang, Y. Gu, W. Wang, X. Jin, J. Zhou, Contact electrification induced multicolor self-recoverable mechanoluminescent elastomer for wearable smart light-emitting devices, Adv. Opt. Mater. 11 (2023) 2203112.
[143] F. Wang, K. Yao, C. Chen, K. Wang, H. Bai, X.-L. Hao, Q. Wang, X. Dong, W. Liu, Lanthanide-coordinated multifunctional hydrogel for detecting human motion and encrypting information, Adv. Funct. Mater. 35 (2025) 2418373.
[144] C. Alexander, Z. Guo, P.B. Glover, S. Faulkner, Z. Pikramenou, Luminescent lanthanides in biorelated applications: from molecules to nanoparticles and diagnostic probes to therapeutics, Chem. Rev. 125 (2025) 2269–2370.
[145] W. Li, Z. Liang, P. Wang, Q. Ma, The luminescent principle and sensing mechanism of metal-organic framework for bioanalysis and bioimaging, Biosens. Bioelectron. 249 (2024) 116008.
[146] R. Sivakumar, N.Y. Lee, Recent advances in luminescent lanthanides and transition metal complex-based probes for imaging reactive oxygen, nitrogen, and sulfur species in living cells, Coord. Chem. Rev. 501 (2024) 215563.
[147] R. Sánchez-Fernández, I. Obregon-Gomez, A. Sarmiento, M.E. Vásquez, E. Pazos, Luminescent lanthanide metallopeptides for biomolecule sensing and cellular imaging, Chem. Commun. 60 (2024) 12650–12661.
[148] Y. Liu, Y. Lu, X. Yang, X. Zheng, S. Wen, F. Wang, X. Vidal, J. Zhao, D. Liu, Z. Zhou, C. Ma, J. Zhou, J.A. Piper, P. Xi, D. Jin, Amplified stimulated emission in upconversion nanoparticles for super-resolution nanoscopy, Nature 543 (2017) 229–233.

[149] J. Zhou, A.I. Chizhik, S. Chu, D. Jin, Single-particle spectroscopy for functional materials, Nature 579 (2020) 41–50.
[150] L. Liang, Z. Feng, Q. Zhang, T.D. Cong, Y. Wang, X. Qin, Z. Yi, M.J.Y. Ang, L. Zhou, H. Feng, B. Xong, M. Gu, X. Li, X. Liu, Continuous-wave near-infrared stimulated-emission depletion microscopy using downshifting lanthanide nanoparticles, Nat. Nanotechnol. 16 (2021) 975–980.
[151] B. Liu, J. Liao, Y. Song, C. Chen, L. Ding, J. Lu, J. Zhou, F. Wang, Multiplexed structured illumination super-resolution imaging with lifetime-engineered upconversion nanoparticles, Nanoscale Adv. 4 (2022) 30–38.
[152] S. Lamon, H. Yu, Q. Zhang, M. Gu, Lanthanide ion-doped upconversion nanoparticles for low-energy super-resolution applications, Light Sci. Appl. 13 (2024) 252.
[153] E.L. Schmidt, Z. Ou, E. Ximendes, H. Cui, C.H.C. Keck, D. Jaque, G. Hong, Near-infrared II fluorescence imaging, Nat. Rev. Meth. Primers 4 (2024) 23.
[154] Y. Ning, J. Tang, Y.-W. Liu, J. Jing, Y. Sun, J.-L. Zhang, Highly luminescent, biocompatible ytterbium(III) complexes as near-infrared fluorophores for living cell imaging, Chem. Sci. 9 (2018) 3742–3753.
[155] Z.-H. Chen, B. Yun, Y. Hou, X. Wang, X. Wang, J. Xu, L. Jiang, T. Han, H. Zhang, F. Zhang, NIR-II anti-stokes luminescence nanocrystals with 1710 nm excitation for in vivo bioimaging, Angew. Chem. Int. Ed. 64 (2025) e202416893.
[156] Y. Liu, H. Yin, Y. Luo, Y. Luo, L. Jiang, D. Gallego-Ortega, Y.Y. Cheng, P.A. Gale, G. Bao, Lanthanide-doped nanoprobes for microRNA detection, Coord. Chem. Rev. 536 (2025) 216644.
[157] X. Jiang, C. Hao, H. Zhang, X. Wu, L. Xu, M. Sun, C. Xu, H. Kuang, Dual-modal Fe_xCu_ySe and upconversion nanoparticle assemblies for intracellular MicroRNA-21 detection, ACS Appl. Mater. Interfaces 12 (2021) 41405–41413.
[158] T. Zhao, X. Sun, J. Chen, D. Li, W. Cao, S. Chen, Y. Yin, S. Xu, X. Luo, Optically programmable plasmon enhanced fluorescence-catalytic hairpin assembly signal amplification strategy for spatiotemporally precise imaging, Anal. Chem. 94 (2022) 5399–5405.
[159] H. Yu, P.F. Xu, Y. Liu, Z.-S. Jia, Y.-Y. Li, H.-W. Tang, LRET-based simultaneous detection of dual miRNAs via multitrap optical tweezers assisted suspension array tagged by two different luminescent quenchable UCNPs combining CRISPR/Cas12a amplification, Anal. Chem. 97 (2025) 602–612.
[160] F. Zhai, B. Yun, J. Ming, T. Yu, B. Li, X. Liu, X. Wang, Z.H. Chen, C. Song, M. Zhao, W. Li, Z. Liu, A. Liang, J. Li, F. Zhang, Non-invasive diagnosis of early colorectal cancerization via amplified sensing of MicroRNA-21 in NIR-II window, Adv. Mater. 37 (2025) 2501378.
[161] M. Dekaliuk, N. Hildebrandt, Lanthanide-FRET molecular beacons for microRNA biosensing, logic operations, and physical unclonable functions, Eur. J. Inorg. Chem. 26 (2023) e202300288.
[162] X. Wang, K. Gopalsamy, G. Clavier, G. Maurin, B. Ding, A. Tissot, C. Serre, Lanthanide MOF-based luminescent sensor arrays for the detection of castration-resistant prostate cancer curing drugs and biomarkers, Chem. Sci. 15 (2024) 6488–6499.
[163] N. Sayyadi, I. Justiniano, R.E. Connally, R. Zhang, B. Shi, L. Kautto, A.V. Everest-Dass, J. Yuan, B.J. Walsh, D. Jin, R.D. Willows, J.A. Piper, N.H. Packer, Sensitive time-gated immunoluminescence detection of prostate cancer cells using a TEGylated Europium ligand, Anal. Chem. 88 (2016) 9564–9571.
[164] Y. Shi, B. Shi, A. Dass, Y. Lu, N. Sayyadi, L. Kautto, R.D. Willows, R. Chung, J. Piper, H. Nevalainen, B. Walsh, D. Jin, N.H. Packer, Stable upconversion nanohybrid particles for specific prostate cancer cell immunodetection, Sci. Rep. 6 (2016) 37533.
[165] R. Lengacher, K.E. Martin, D. Smilowicz, H. Esseln, P. Lotlikar, A. Grichine, O. Maury, E. Boros, Targeted, molecular Europium(III) probes enable luminescence-guided surgery and 1 photon post-surgical luminescence microscopy of solid tumors, J. Am. Chem. Soc. 145 (2023) 24358, 24336.
[166] K. Ge, G. Chen, D. Zhang, J.-N. Hao, Y. Li, Leap-Type response of Redox/photo-active lanthanide-based metal-organic frameworks for early and accurate screening of prostate cancer, Angew. Chem. Int. Ed. 63 (2024) e202411956.
[167] Z. Luo, D. Mao, X. Li, J. Luo, C. Gong, X. Liu, Lanthanide-based nanoparticles for cancer phototherapy, Coord. Chem. Rev. 508 (2024) 215773.
[168] C. Xie, H.-F. Chau, J.-X. Zhang, S. Tong, L. Jiang, W.-Y. Fok, H.-L. Lung, S. Zha, R. Zou, J. Jiao, C.-F. Ng, P.A. Ma, J. Zhang, J. Lin, K.K. Shiu, J.-C.G. Bünzli, W. W. Wong, N.J. Long, G.-L. Law, K.-L. Wong, Bladder cancer photodynamic therapeutic agent with Off-On magnetic resonance imaging enhancement, Adv. Therap. 2019 (2019) 1900068.
[169] P. Du, Y. Wei, Y. Liang, R. An, S. Liu, P. Lei, H. Zhang, Near-infrared-responsive rare Earth nanoparticles for optical imaging and wireless phototherapy, Adv. Sci. (2023) 2305308.
[170] H. Li, P. Li, J. Zhang, Z. Lin, L. Bai, H. Shen, Applications of nanotheranostics in the second near-infrared window in bioimaging and cancer treatment, Nanoscale 16 (2024) 21697.
[171] D. Maiti, H. Yu, Y. Mocida, S. Won, S. Yamashita, M. Naito, K. Miyata, H.J. Kim, Terbium-rose bengal coordination nanocrystals-induced ROS production under low-dose X-rays in cultured cancer cells for photodynamic therapy, ACS Appl. Bio Mater. 6 (2023) 2505–2513.
[172] Y. An, D. Xu, P. He, Z. Wang, Y. Li, J. Ming, R. Liu, J. Li, Z. Lu, G. Liu, A lanthanide nanoparticle-aggregation-induced emission photosensitizer complex system drives coupled triplet energy transfer for enhanced radio-photodynamic therapy, J. Am. Chem. Soc. 147 (2025) 11964–11974.
[173] J. Li, S. Lyu, C.A. Li, Y. Tang, F. Wang, Q. Wang, X. Li, G. Xu, H. Li, Y. Zhang, Z. Guo, X. Chen, X. Zhang, Radionuclide-activated luminescence for cancer theranostics, Chem. Eur J. 31 (2025) e202500296.
[174] D. Maiti, H. Yu, Y. Mochida, S. Won, S. Yamashita, M. Naito, K. Miyata, H.J. Kim, Terbium-rose bengal coordination nanocrystals-induced ROS production under low-dose X-rays in cultured cancer cells for photodynamic therapy, ACS Appl. Bio Mater. 6 (2023) 2505–2513.
[175] D. Maiti, H. Yu, J. S, An, S. Yamashita, M. Naito, K. Miyata, H.J. Kim, Dual porphyrin-loaded scintillating nanoparticles enhanced photodynamic therapy in hypoxic cancer cells under X-ray irradiation, Chembiochem 26 (2025) e202400838.
[176] L. Lei, Y. Wang, A. Kuzmin, Y. Hua, J. Zhao, S. Xu, P.N. Prasad, Next generation lanthanide doped nanoscintillators and photon converters, Light Sci. Appl. 2 (2022) 2–17.
[177] B. Hou, L. Yi, D. Hu, Z. Luo, D. Gao, C. Li, B. Xing, J.-W. Wang, C.N. Lee, R. Zhang, Z. Sheng, B. Zhou, X. Liu, A swallowable X-ray dosimeter for the real-time monitoring of radiotherapy, Nat. Biomed. Eng. 7 (2023) 1242–1251.
[178] Y. Sun, M. Kong, J. Ke, Y. Gu, F. Li, W. Feng, Rare earth luminescent nanothermometers for biological thermal sensing, Coord. Chem. Rev. 523 (2025) 216222.
[179] A.M. Kaczmarek, H.S. Jena, C. Krishnaraj, H. Rijckaert, S.K.P. Veerapandian, A. Meijerink, P. Van Der Voort, Luminescent ratiometric thermometers based on a 4f-3d grafted covalent organic framework to locally measure temperature gradients during catalytic reactions, Angew. Chem. Int. Ed. 60 (2021) 3727–3736.
[180] E.P. Santos, R.S. Pugina, E.G. Hilario, A.J.A. Carvalho, C. Jacinto, F.A.M.G. Rego-Filho, A. Canabarro, A.S.L. Gomes, J.M.A. Caiut, A.L. Moura, Towards accurate real-time luminescence thermometry: an automated machine learning approach, Sens. Actuators A Phys. 362 (2023) 114666.
[181] C. Kränkel, D.-T. Marzahl, F. Moglia, G. Huber, P.W. Metz, Out of the blue: semiconductor laser pumped visible rare-earth doped lasers, Laser Photon. Rev. 10 (2016) 548–568.
[182] J.-X. Zhang, C. Wang, Y.-F. Li, Y. Yu, Y. Wang, Z. Lv, Research status of rare-earth-ion doped infrared lasers, Front. Physiol. 12 (2024) 1388567.
[183] C. Zhang, Q. Yin, S. Ge, J. Qi, Q. Han, W. Gao, Y. Wang, M. Zhang, J. Dong, Optical anti-counterfeiting and information storage based on rare-earth-doped luminescent materials, Mater. Res. Bull. 176 (2024) 112801.
[184] G. Swati, S. Mishra, Luminescent nanomaterials for developing high-contrast latent fingerprints, Nanotechnology 36 (2025) 032001.
[185] Z. Yang, J.J. Joos, J. Hu, D. Van der Heggen, T. Pier, M. Delaey, H. Vrielinck, T. Jüstel, P.F. Smet, D. Poelman, Personal solar UV monitoring based on photoinduced electron transfers in luminescent materials, Adv. Opt. Mater. 11 (2023) 202300733.
[186] J.H.S.K. Monteiro, N.R. Fetto, M.J. Tucker, F.A. Sigoli, A. de Bettencourt-Dias, Carbazole-functionalized dipicolinato Ln(III) complexes show two-photon excitation and viscosity-sensitive metal-centered emission, J. Lumin. 245 (2022) 118768.
[187] F. Ngom, A. Chang, C. Blais, C. Daiguebonne, Y. Suffren, M. Camara, G. Calvez, K. Bernot, O. Guillou, Halogen-bonds-based strategy for the design of highly luminescent lanthanide coordination polymers as taggants for plastic waste sorting, Inorg. Chem. 63 (2024) 13048–13058.
[188] P. Mena-Giraldo, M. Kaur, S.L. Maurizio, G.A. Mandl, J.A. Capobianco, Janus micromotors for photophoretic motion and photon upconversion applications using a single near-infrared wavelength, ACS Appl. Mater. Interfaces 16 (2024) 4249–4260.
[189] D.W. Kim, P. Wrede, A.R. Rodriguez-Camargo, Y. Chen, N.O. Dogan, C. Glück, B. V. Lotsch, D. Razansky, M. Sitti, Upconversion nanoparticle-covalent organic framework core-shell particles as therapeutic microrobots trackable with optoacoustic imaging, Adv. Mater. 37 (2025) 2418425.
[190] G. Chen, M. Zhu, D. Zhong, J. Liu, Y. Li, Y. Zang, S. Sun, H. Liu, S. Wang, Y. Xin, X. Wang, C. Hu, B. Teng, Transparent and thermally stable rare-earth-doped luminescent gallate glass toward passive daytime radiative cooling applications, Inorg. Chem. 63 (2024) 21507–21518.
[191] M.T. Uysal, L. Dusanowski, H. Xu, S.P. Horvath, S. Ourri, R.J. Cava, N.P. de Leon, J.D. Thompson, Spin-photon entanglement of a single Er^{3+} ion in the telecom band, Phys. Rev. X 15 (2025) 011071.
[192] M.-L. Cai, Z.-D. Liu, W.-D. Zhao, Y.-K. Wu, Q.-X. Mei, Y. Jiang, L. He, X. Zhang, Z.-C. Zhou, L.-M. Duan, Observation of a quantum phase transition in the quantum Rabi model with a single trapped ion, Nat. Commun. 12 (2021) 1126.
[193] J. Zhang, P.W. Hess, A. Kyprianidis, P. Becker, A. Lee, J. Smith, G. Pagano, I.-D. Potirniche, A.C. Potter, A. Viswanath, N.Y. Yao, C. Monroe, Observation of a discrete time crystal, Nature 543 (2017) 217–220.
[194] M.P. Hehlen, M. Sheik-Bahae, R.I. Epstein, Solid-state optical refrigeration, in: J.-C.G. Bünzli, V.K. Pecharsky (Eds.), Handbook on the Physics and Chemistry of Rare Earths, vol. 45, Elsevier Science B.V., 2014, pp. 179–260. Ch. 265.
[195] J. Thomas, L. Maia, Y. Ledemi, Y. Messaddeq, R. Kashyap, Emerging trends, challenges, in: A. Ray (Ed.), Applications in Solid-State Laser Cooling in *Oxide Electronics*, vol. 10, John Wiley & Sons Ltd, 2021, pp. 353–396.
[196] G. Tessitore, G.A. Mandl, S.L. Maurizio, M. Kaur, J.A. Capobianco, The role of lanthanide luminescence in advancing technology, RSC Adv. 13 (2023) 17787–17811.
[197] C. Yan, X. He, B. Yu, B. Zhou, S. Fang, J. Xu, B. Liu, Z. Wang, A mechanoluminescence-based stress sensing hydrogel for intelligent artificial ligament, Adv. Funct. Mater. 35 (2025) 2420142.
[198] S. Geng, H. Li, Z. Lv, Y. Zhai, B. Tian, Y. Luo, Y. Zhou, S.-T. Han, Challenges and opportunities of upconversion nanoparticles for emerging NIR optoelectronic devices, Adv. Mater. (Weinheim, Ger.) 37 (2025) 2419678.

Update

Journal of Luminescence
Volume 289, Issue , January 2026, Page

DOI: https://doi.org/10.1016/j.jlumin.2025.121614

Journal of Luminescence 289 (2026) 121614

Contents lists available at ScienceDirect

Journal of Luminescence

journal homepage: www.elsevier.com/locate/jlumin

Corrigendum

Corrigendum to "Lanthanide photonics on the path to future: from gas lighting to optical computers" [J. Lumin. 287 (2025) 121473]

Jean-Claude G. Bünzli [a,b,*], Ka-Leung Wong [a]

[a] Hong Kong Polytechnic University, Department of Applied Biology and Chemical Technology, Hung Hom, Hong Kong Special Administrative Region of China
[b] Swiss Federal Institute of Technology, Lausanne (EPFL), Institute of Chemical Sciences and Engineering, Lausanne, Switzerland

The authors regret that during proofreading they oversaw that the labels in Figure 11a have been changed during typesetting. The correct Figure 11a is reproduced below

Fig. 11. a) Energy diagram for Pr^{3+} with GSA and ESA processes; Redrawn from ref. [63].

In addition, the graphical abstract is missing from the final version of the paper:

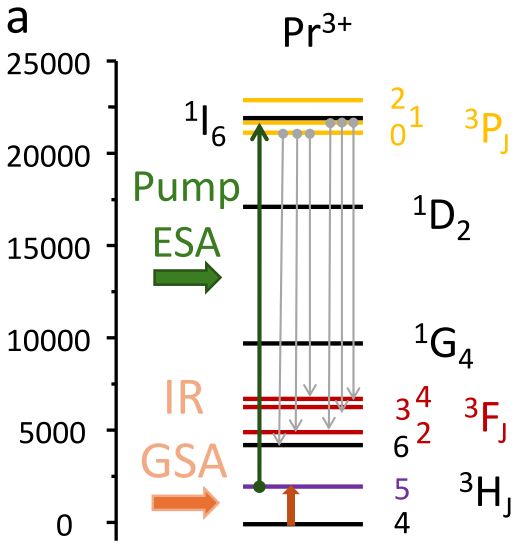

DOI of original article: https://doi.org/10.1016/j.jlumin.2025.121473.
* Corresponding author. Hong Kong Polytechnic University, Department of Applied Biology and Chemical Technology, Hung Hom, Hong Kong Special Administrative Region of China.
E-mail address: jean-claude.bunzli@epfl.ch (J.-C.G. Bünzli).

https://doi.org/10.1016/j.jlumin.2025.121614

Available online 19 October 2025

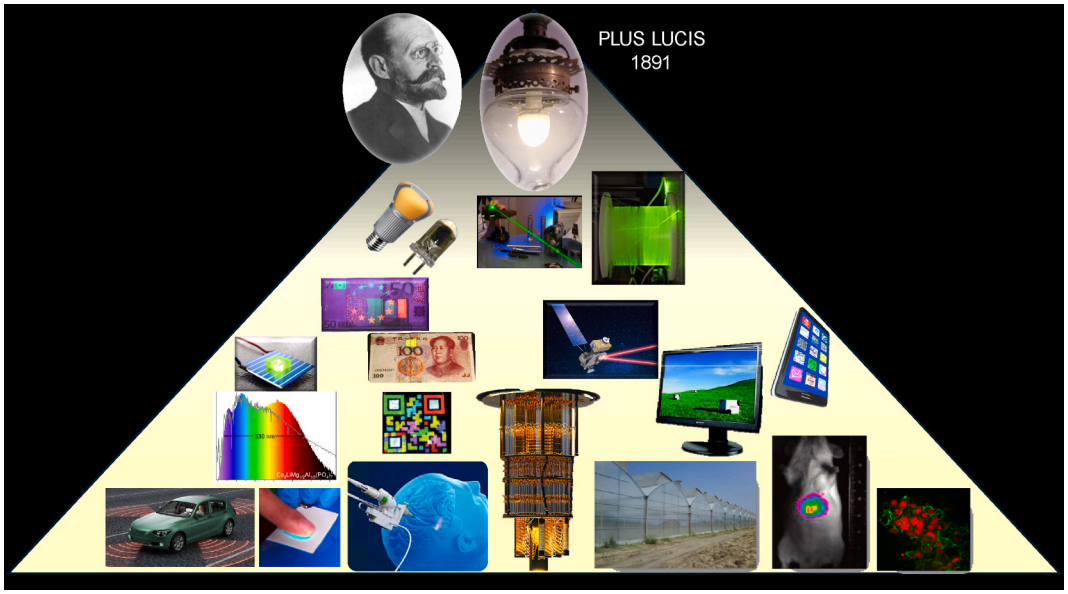

The authors would like to apologise for any inconvenience caused by these technical errors.